DESIGN AND DEVELOPMENT OF A COHERENT DETECTION RAYLEIGH DOPPLER LIDAR SYSTEM FOR USE AS AN ALTERNATIVE VELOCIMETRY TECHNIQUE IN WIND TUNNELS

Thesis

Submitted to

The School of Engineering of the

UNIVERSITY OF DAYTON

In Partial Fulfillment of the Requirements for

The Degree of

Master of Science in Aerospace Engineering

By

Samuel Adam Barnhart, B.S.

Dayton, Ohio

August 2020

DEVELOPMENT OF A COHERENT DETECTION RAYLEIGH DOPPLER LIDAR SYSTEM FOR USE AS AN ALTERNATIVE VELOCIMETRY TECHNIQUE IN WIND TUNNELS

Name: Barnhart, Samuel Adam

APPROVED BY:

Sidaard Gunasekaran, PhD.
Advisory Committee Chairman
Assistant Professor
Department of Mechanical
and Aerospace Engineering

Aaron Altman, PhD.
Committee Member
Graduate Faculty
Department of Mechanical
and Aerospace Engineering

Paul McManamon, PhD.
Committee Member
Professor
Department of Electro-Optics

Robert J. Wilkens, Ph.D., P.E.
Associate Dean for Research and Innovation
Professor
School of Engineering

Eddy M. Rojas, Ph.D., M.A., P.E.
Dean, School of Engineering

ABSTRACT

DESIGN AND DEVELOPMENT OF A COHERENT DETECTION RAYLEIGH DOPPLER LIDAR SYSTEM FOR USE AS AN ALTERNATIVE VELOCIMETRY TECHNIQUE IN WIND TUNNELS

Name: Barnhart, Samuel Adam
University of Dayton

Advisor: Dr. Sidaard Gunasekaran

Velocity measurement inside of a wind tunnel is an extremely useful quantitative data for a multitude of reasons. One major reason is that velocity has a mathematical relationship with dynamic pressure which in turn influences all the aerodynamic forces on the test model. Many devices and methods exist for measuring velocity inside wind tunnels. At the same time, Doppler wind lidar (light detection and ranging) has been used for decades to make air speed measurements outdoors at long ranges. Lidar has been proven effective for many applications, and it has the potential to solve many of the problems faced by current velocimetry techniques inside wind tunnels. Despite this, minimal research has been performed with Doppler wind lidars inside wind tunnels. While multiple commercial systems exist for making air speed measurements at longer ranges, there are currently no widely available commercial devices designed to work well inside wind tunnels.

In this research, initial work is described for the design and development of a continuous wave (CW), coherent wind lidar system. The system is for use as an alternative non-intrusive velocimetry method inside wind tunnels relying on the Doppler effect. A scaled down wind lidar designed to operate at much shorter ranges than current commercial

wind lidars can be simpler, less expensive, and require less power. A first iteration of the design was constructed for proof of concept testing with a small-scale wind tunnel at low speeds (7.5-9 m/s). Testing showed that the lidar system could take one-dimensional speed measurements of seeded flow that closely matched Pitot static tube data. When not adding tracer particles to the flow, the lidar return signal was not strong enough for the photodetector used to measure the beat frequency.

This research is focused on the process for designing the Doppler wind lidar system, constructing the experimental setup, and studying methods for data analysis. Results of testing presented in the paper and lessons learned were used to create a second iteration of the wind lidar design that can be built for future testing. Not all data analysis methods and experiments described herein were successful, but this documentation will be helpful to future researchers for improving the design and continuing to make progress on a much needed device for wind tunnel velocimetry.

This thesis is dedicated to all those about to try something new. Do not be afraid to fail –

Just learn from it.

ACKNOWLEDGEMENTS

I would first like to thank my advisor, Dr. Sidaard Gunasekaran, for being extremely supportive of me throughout my undergraduate and graduate career at the University of Dayton. He pushed me to keep working hard throughout this project and helped me develop a lifelong love for learning. The following members of the Electro-Optics & Photonics Department and the Ladar Optical Communication Institute have been extremely helpful to learn lidar including Edward Ruff, Cullen Bradley, Andrew Reinhardt, and Dr. Paul McManamon. Their advice and patience with me as I worked in their lab was critical in ensuring that my research was successful. Finally, I am extremely appreciative of all friends and family who supported me in many ways that I can never imagine. I am forever in debt to all of you.

This material is based on research sponsored by the Ohio Department of Higher Education and the Southwestern Council for Higher Education under Ohio House Bill 49 of the 132nd General Assembly. The U.S. Government is authorized to reproduce and distribute reprints for Governmental purposes notwithstanding any copyright notation thereon. The views and conclusions contained herein are those of the authors and should not be interpreted as necessarily representing the official policies or endorsements, either expressed or implied, of Southwestern Council for Higher Education, the Ohio Department of Higher Education or the U.S. Government

TABLE OF CONTENTS

LIST OF FIGURES

LIST OF SYMBOLS/ABBREVIATIONS

A	Receiver Area
AFIT	Air Force Institute of Technology
AFRL	Air Force Research Laboratory
APD	Avalanche Photodetector
BD	Beam Dump
c	Speed of Light
CW	Continuous Wave
d_f	Fringe Distance
d_P	Particle Diameter
DFT	Discrete Fourier Transform
DTU	Denmark Technical University
E_{LO}	Electric Field of Signal
E_{sig}	Electric Field of LO
E_λ	Energy of a Photon
f_{beat}	Beat Frequency
$f_{Doppler}$	Doppler Frequency
f_{Laser}	Laser Frequency
f_{sig}	Signal Frequency
FFT	Fast Fourier Transform
G	Range-Dependent Geometry
h	Planck's Constant

I	Electric Field Output Intensity
K	Lidar System Performance
l_0	Obstacle Diameter
LADAR	Laser Detection and Ranging
LDV	Laser Doppler Velocimetry
LEEDR	Laser Environmental Effects Definition and Reference
LIDAR	Light Detection and Ranging
LO	Local Oscillator
LOCI	Ladar Optical Communications Institute
N	Number of Data Points
N_j	Scattering Particle Concentration
N_0	Number of Photons Output
O	Receiver-Field-of-View Overlap Function
P	Lidar Return Power
P_0	Lidar Output Power
P_s	Static Pressure
P_t	Total Pressure
PD	Photodetector
PIV	Particle Image Velocimetry
q	Dynamic Pressure
R	Measurement Range
RADAR	Radio Wave Detection and Ranging
RF	Reflective Filter

SNR	Signal to Noise Ratio
SODAR	Sound Detection and Ranging
SONAR	Sound Detection and Ranging
Stk	Stokes Number
T	Transmission Coefficient
UV	Ultraviolet
V_{LOS}	Line of Sight Velocity
V_P	Particle Velocity
v_r	Voltage Sequence
V_∞	Freestream Velocity
w_0	Laser Beam Waist
WPAFB	Wright Patterson Air Force Base
α	Extinction Coefficient
β	Backscatter Coefficient
β_m	Backscatter Coefficient per Unit Volume
Γ	Probe Length
Δf	Doppler Shift
Δt	Time of Flight
η	System Efficiency
θ	Angle Between Laser and Air Velocity
λ	Laser Wavelength
μ	Dynamic Viscosity
ρ	Air Density

ρ_P	Particle Density
$\frac{d\sigma_j}{d\Omega}$	Scattering Cross Section
τ	Time Interval
ω_{LO}	Spatial Frequency of the LO
ω_{sig}	Spatial Frequency of Signal

CHAPTER I

INTRODUCTION

1.1 Problem Statement

People desire to measure air speeds for many reasons, encompassing applications from HVAC to meteorology and renewable energies. Measuring air speeds can help to better understand the fluid flow for research, design, and process monitoring. Most of these applications require only a time averaged velocity measurement with minimal restrictions on the measurement uncertainty. Something as simple as a cup anemometer can be used to achieve this goal.

Air speed measurements inside wind tunnels must frequently be made with sufficient accuracy and precision. For example, ambient turbulence intensity measurements inside a wind tunnel require velocity measurements with uncertainty within a fraction of a percentage of the freestream velocity. Researchers use a plethora of tools for measuring the velocity of air in a wind tunnel. Instead of directly measuring the velocity, most devices measure a different flow property (such as pressure or temperature) and use it to calculate velocity based on known relations and calibrations. Each device has its advantages and disadvantages based on the process used to determine air speed. Some are simple to use while others are complex; some are cheap while others are expensive; some are accurate while others are not; some have a high bandwidth while others are slow; some include many assumptions about the flow while others include less. There is currently no ideal instrument for all velocity measurement requirements inside a wind tunnel. One method minimally used for wind tunnel velocity measurements to date is lidar. While lidar

likely cannot be the ideal instrument for all wind tunnel velocity measurements, it has potential to overcome many of the disadvantages faced by other methods. The ultimate reason being that lidar measures wind velocity directly without relying on any other flow properties. In this chapter, multiple common methods for determining the air speed in a wind tunnel are described. Afterwards, lidar is proposed as an alternative method to be developed for use as a potentially superior method.

1.2 Current velocimetry techniques

One common device for measuring the freestream air speed is the Pitot-static tube. A hole in the front of the tube measures stagnation (or total) pressure, P_t while a hole on the side of the tube measures static pressure, P_s. The difference between these two values is dynamic pressure, q, defined in a simplified version of Bernoulli's equation as

$$P_t - P_s = q = \frac{1}{2}\rho V_\infty^2 \tag{1}$$

where ρ is the air density and V_∞ is the freestream speed. With q and ρ known, the freestream speed can be solved for [1]. While Bernoulli's equation is generally useful in this application, it has several inherent assumptions such as inviscid flow, steady flow, incompressible flow, constant total pressure, irrotational or applicable to a single streamline if the flow is rotational. Due to these assumptions, a Pitot static tube is only useful under conditions that meet the assumptions. Fortunately, the wind tunnels are designed so that most of these assumptions hold true for the Bernoulli equation and the Pitot tube or Prandtl tube to be applicable. However, determining an ideal location to mount the Pitot tube in a wind tunnel is a challenging endeavor for a variety of reasons. [2]

Pitot static tubes are mounted onto most aircraft for air speed measurements that are relayed to the pilot. These measurements are time averaged and useful for steady flow but cannot quantify unsteady pressures. Additionally, pressure probes such as the Pitot static tube are highly sensitive to yaw angle and do not properly measure the pressure when not mounted parallel with the flow. This can be problematic when the flow is turbulent because the flow is no longer travelling in a consistent direction. Pitot static tubes will only measure the mean velocity of a turbulent flow. Similarly, when the probe is mounted inside of a shear layer where the flow velocity is not consistent across the probe, the device is not useful for measuring the change in velocity. Despite being a simple and inexpensive device, Pitot static tubes have many sources of error. Even when properly used to minimize these errors, the devices still have an uncertainty of about 0.1 m/s. [2] While some applications allow an uncertainty of 0.1 m/s, this is not always the case.

Another common device for measuring air flow speeds is a hot wire anemometer. A heated wire, generally only a few μm in diameter (easily broken by dust in the air), is inserted into the flow [3]. The moving air cools the wire via convection and changes the wire resistance from a known value. At the same time, heat is generated in the wire when current travels through it. Matching the convection with current to maintain a consistent temperature, the voltage applied to the probe is measured. The probe is calibrated to associate changes in resistance with velocities. Calibration must be performed before each use of the hot wire anemometer because the metal wire is very susceptible to ambient temperature changes in addition to Reynolds number, Mach number, and the Knudsen number. If the anemometer is not properly calibrated, the measurements will not be accurate. One advantage of these probes is that they can be operated at high speeds. This

is useful for measuring the turbulence intensity of a wind tunnel and unsteady flows. Finally, hot wire anemometers must be carefully mounted like Pitot static tubes to have a known angle with the flow. If testing is performed properly to minimize error, the velocity measurements are more accurate than Pitot static tubes with uncertainty as low as about 0.015 m/s. [4]

Both techniques can measure air speed with a relatively small cost, but they depend upon indirectly determining the air speed through pressure and temperature measurements. Additionally, they are intrusive techniques that require putting an object into the flow. Doing this will disrupt the flow (including disruptions propagating upstream at subsonic speeds) and potentially interfere with results. If mounted inside a wind tunnel too close to a wing or other object of interest, the modified flow field caused by the Pitot tube or hot wire anemometer probe changes the performance of the wing. Similarly, Pitot static tubes cannot be mounted close to test articles because these models are disturbing the flow and would change measurement results (usually leading to an overestimation of the air speed). Additionally, it may not be possible to physically reach the flowfield of interest with these devices to measure the flow. This research focuses on the development of a nonintrusive velocimetry technique. Two common nonintrusive, optical, velocimetry techniques used in wind tunnels that rely on the use of laser beams in the flow are particle image velocimetry (PIV) and laser Doppler velocimetry (LDV).

The basic concept of the PIV technique is to seed the flow with tracer particles which are of very small size (usually on the order of μm) such as Roscoe fluid, glycerin based seed, olive oil, talc, titanium dioxide, phenolic resin or others depending on the medium. The components used in PIV are shown in Figure 1. [5] This technique uses a

high power pulsed laser (usually class IV) to illuminate the seed. A plano-convex lens is used to spread the laser beam into a planar sheet which illuminates the tracer particles in the desired area of the test section. The particles will produce Mie scattering since they are similar in size to the wavelength of the laser.

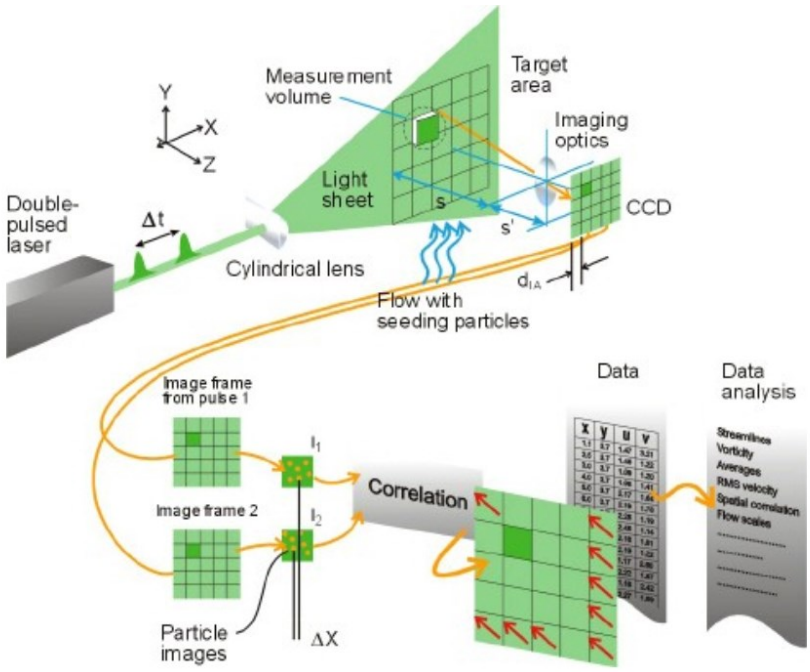

Figure 1. The typical setup used for particle image velocimetry in a wind tunnel. [5]

A high speed camera is used to capture separate images of the scattered light with each light pulse. The processing of the images is done by dividing the recorded images into subsections called interrogation regions. The interrogation regions from each image are correlated with each other pixel by pixel. The correlation produces a signal peak identifying the displacement of the particle within the image pair. To convert this displacement to a physical distance travelled by the particles, the image is calibrated to know how many pixels equate to a representative length within the camera's field of view. The calculated

particle displacement is then converted into velocity by using the time between the images. The correlation and velocity calculation process in each interrogation region is repeated throughout the entire image to generate an overall velocity contour map like the one shown in Figure 2. [6] In this example, the PIV technique was able to capture the wake behind the wing of a model commercial aircraft. A clear wingtip vortex is visible at $y = -500$ and $z = 25$. If the PIV setup was rotated 90° to capture the wake behind the wing as it moves downstream, the drag coefficient per unit span could be calculated.

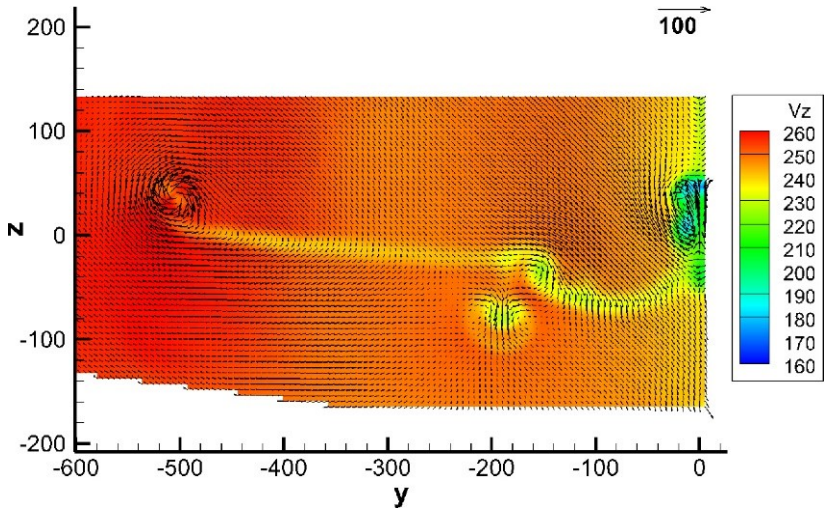

Figure 2. PIV can generate velocity contour maps of flow in a wind tunnel. [6]

PIV is a difficult process to perform well in a wind tunnel to achieve accurate velocity results like those in Figure 2. Multiple equipment including a laser and camera must be mounted at the proper distance apart and perpendicular to each other when performing classical PIV. This mounting varies with the wind tunnel used and the flowfield being tested, so a custom setup must be determined for each use. Additionally, the camera must focus onto the laser light sheet with a small depth of field to image only the

illuminated particles. These illuminated particles must be the proper size/density and evenly distributed throughout the flow. If the laser does not have the proper power, the tracer particles may either be illuminated too much or not enough for detection by the camera. If the improper filters are applied to the data during postprocessing, the results may be artificially skewed. The chart in Figure 3 highlights the different sources of error that can occur in PIV. Performing this velocimetry technique well takes years of practice and is as much an art as it is a science. Many of these error sources are assumed negligible in research papers, but the errors frequently stack up to a cumulative error that can make results useless, depending upon the application's accuracy requirements.

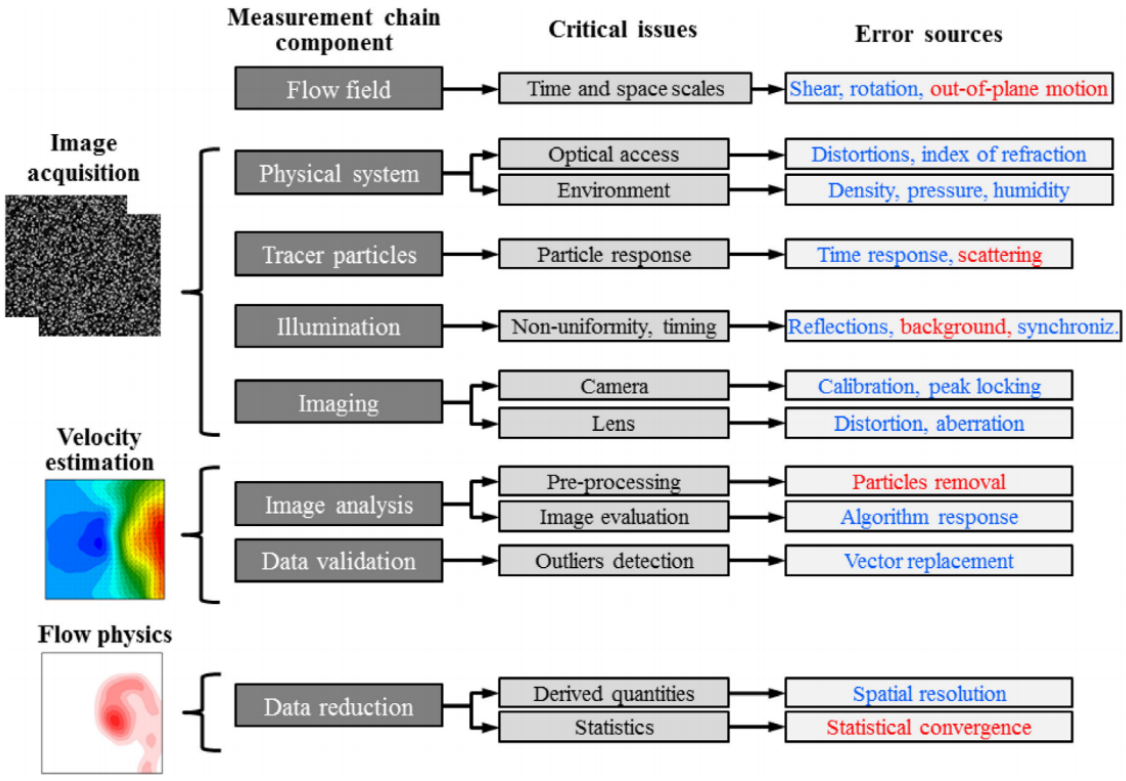

Figure 3. The many types of error possible in PIV can lead to a large cumulative error. *[7]*

Like PIV, LDV also requires seeding to measure velocity. While it is a separate technique on its own, LDV suffers from many of the same error sources as PIV. The basic configuration of LDV, shown in Figure 4, consists of a continuous wave laser or a pulsed laser, transmitting optics including a beam splitter and a focusing lens, receiving optics comprising a focusing lens, an interference filter, photo detector, a signal conditioner and a signal processor [8]. The beam splitter splits the laser into two beams of equal intensities. These two beams are made to intersect each other at a desired location. This intersection of the two laser beams produces parallel planes of high and low light intensity called fringes. The fringe distance, d_f, is defined by the wavelength of the laser light, λ, and the angle between the two beams, ϕ.

$$d_f = \frac{\lambda}{2sin\left(\frac{\phi}{2}\right)} \tag{2}$$

When a particle passes through these fringes, it scatters light with a Doppler shift and with a Doppler frequency ($f_{Doppler}$) which is proportional to the velocity component perpendicular to the two laser beams. This scattered light is collected by a receiver lens and focused on a photodetector which converts the photons into an electrical signal to be analyzed. For the purpose of testing in the wind tunnels, an interference filter can be mounted before the photodetector to pass only the required wavelength to the photodetector to remove the noise from the ambient light and from other wavelengths [8].

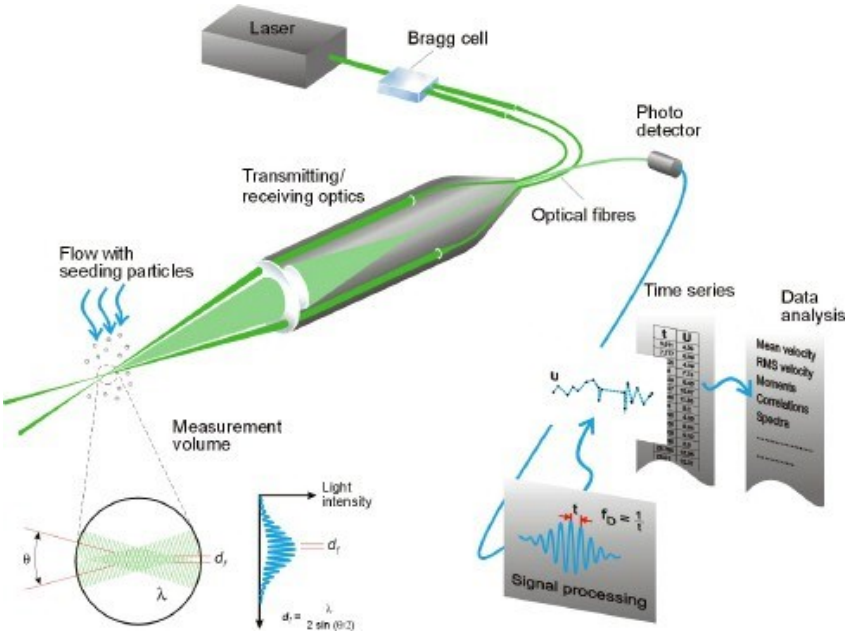

Figure 4. The basic setup for laser Doppler velocimetry as another nonintrusive velocimetry technique [8].

The photodetector then converts the fluctuating light intensity into an electric signal. These signals are filtered and amplified in a signal processor which determines the Doppler frequency for each particle through a Fourier transformation. From spacing of the fringe, d_f, the distance traveled by the particle can be found. From the Doppler frequency, the time it took to go through the fringe can be found ($t = 1/f_{Doppler}$). Therefore from the definition of the velocity, the velocity of the particle is

$$V_P = \Delta f * f_{Doppler} \tag{3}$$

This process is repeated as the system scans throughout the entire region of interest to generate an overall velocity contour map like the one shown in Figure 5. [9] LDV also has some capabilities for three-dimensional velocity measurement. [10]

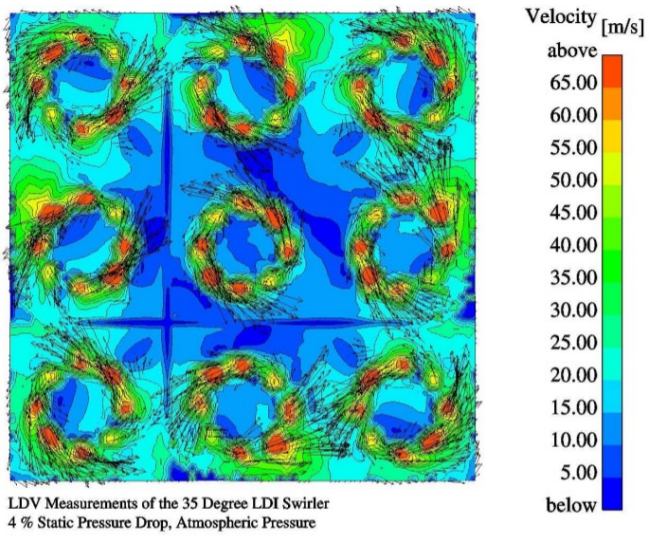

Figure 5. Using LDV, two-dimensional velocity contour plots can be made of flow such as combustion swirlers. [9]

The largest disadvantages of LDV and PIV are that these optical flow diagnostic techniques require seed material to provide the velocity data. This seed material is problematic on numerous levels. Seed material fouls tunnel circuits, interferes with instrumentation, is difficult to distribute uniformly in the flow, and does not necessarily follow the flowfield religiously. A parameter used to show how well a fluid matches fluid flow is the Stokes number, defined as

$$Stk = \frac{\rho_p d_p^2}{18\,\mu}\frac{V_\infty}{l_0} \tag{4}$$

where ρ_p is the tracer particle density, d_p is the particle diameter, μ is the air dynamic viscosity, and l_0 is the diameter of the obstacle in question (or other representative length scale). A Stokes number much less than unity means the particle will closely follow the fluid streamlines. A large Stokes number means the particle trajectory will deviate from the fluid streamlines whenever the fluid accelerates. [7] The Stokes number increases with

the square of particle diameter, so small particles are critical for keeping the Stokes number low. The plot in Figure 6 shows the velocity response of several different diameter particles to a change in the fluid velocity. An increase in the particle diameter causes the response time to be much larger. An example of where it is difficult for particles to follow fluid streamlines is in the core of a vortex. The fluid is moving extremely rapidly with lots of acceleration, so tracer particles are often pushed to the outer part of the vortex where they can move with the flow. Additionally, the use of seeding inside combustion chambers is difficult due to the extremely high temperatures involved.

Ideally, researchers have a nonintrusive velocimetry technique that does not require seeding the flow yet can measure velocities with a minimal uncertainty. This research focuses on the development of one such method that uses lidar. Lidar has been used throughout the world for decades with a rich history in many other disciplines. The potential for lidar to be successful inside wind tunnels is clear based on its reliance on the basic physics of waves and a long track record of success elsewhere.

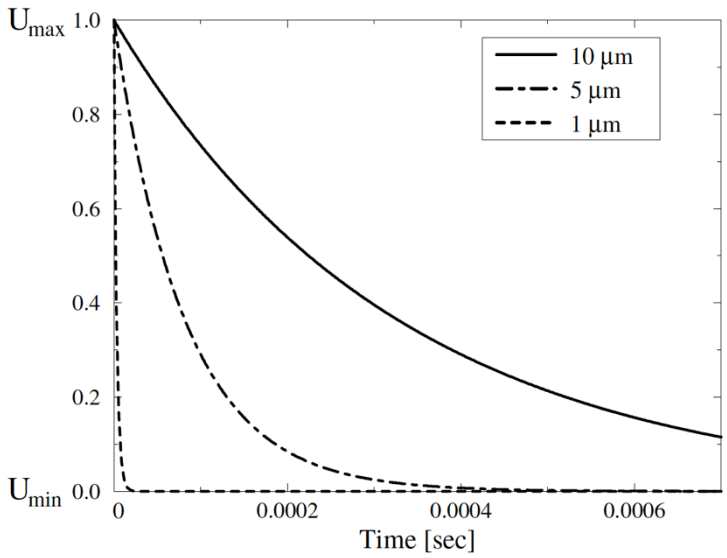

Figure 6. Large diameter particles require much more time to accelerate to fluid flow velocities. *[7]*

1.3 Introduction to lidar

Multiple methods have been developed for detection and ranging of objects including sound detection and ranging (SODAR, also known as SONAR), radio wave detection and ranging (RADAR), and light detection and ranging (LIDAR). Each of these methods include a transmitter that emits electromagnetic waves, either focused or scattered, and a receiver that collects the reflected waves and measures the return with a sensor. Lidar, the focus of this topic, is also known as LIDAR, LiDAR, and LADAR (laser detection and ranging). For consistency, the term lidar will be used in this thesis.

Lidar, as it is known today, began development in the 1960s with the invention of the laser. [11] Research using the same principle of collecting reflected light goes as far back as the 1930s with the use of bright lights such as searchlight beams and flash lamps. [12] [13] [14] [15] This work focused on analysis of clouds and other meteorology development. In 1953, the term lidar was keyed by Middleton and Spilhaus. [16] Sensors such as photomultiplier tubes were already available in 1953, but the light sources were

inadequate due to the lack of power and pulsing capabilities. [17] With the invention of the laser to solve these problems, lidar technology began to quickly evolve, especially within the military. After only a few years, lidar was first used as a rangefinder in the Soviet Union. [11] Books on the topic were first written in the 1970s. [18] In the following decades, lidar technology has developed with electronic and optical technology to become what it is today. Lidar has a wide range of configurations and designs for many uses throughout society.

The illustrations in Figure 7 below show what the basic setup of a lidar system can look like. The transmitter system consists mainly of a laser sending a beam down range. The lasers used are chosen from a wide range of powers (milliwatts to Watts) and wavelengths (ultraviolet to infrared). Additionally, a receiver system collects the light reflected backwards from the object of interest and focuses the light onto a photodetector for measuring the light intensity. Figure 7(a) shows what is called a monostatic setup while part (b) shows a bistatic setup. A bistatic setup has a separate transmitter and receiver as just described. The monostatic design uses a transceiver where the outgoing beam and the return signal are located on the same axis. Since monostatic designs only require one aperture, they can be smaller and light weight. This is helpful because a smaller device will alter the flow less inside a wind tunnel. When working with a monostatic design, the aperture captures all backscattered light (light reflected 180° back towards the lidar system). In order to measure at a specific range, the lidar system must be modified to filter out the light returning from other ranges. A bistatic design can be set up to focus only at a specific range and eliminate this problem.

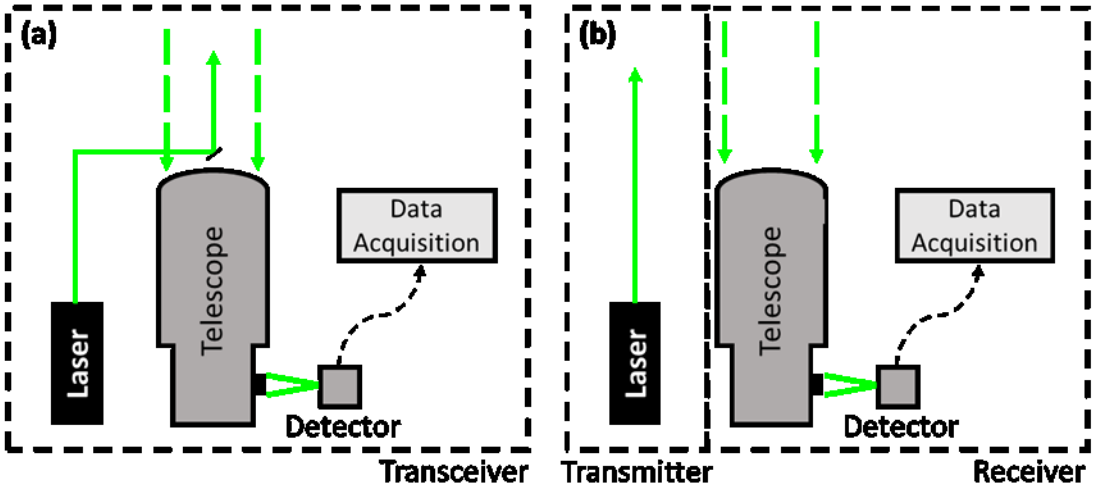

Figure 7. (a) A monostatic lidar setup. (b) A bistatic lidar setup.

When using a photodetector to collect the reflected light, multiple types of information can be gathered. First, the output voltage is directly related to the collected signal strength. Knowing the intensity of the return light can be helpful for identification of the reflecting target. For example, chemicals in the atmosphere can be identified based on their absorption of light. [19] Another type of information that can be gathered is the distance between the lidar system and the target. Since the speed of light, *c,* is well known, we can use the following equation to calculate range to a target

$$R = \frac{c\Delta t}{2} \tag{5}$$

where Δt is the time required for light to travel down range and back to the detector. Lidar ranging can be used with multiple light pulses in fast repetition to measure the velocity of an object. For example, the police use lidar ranging to measure the speed of moving cars. [11]

The type of information that can be gathered depends upon the light detection configuration used. The information described in the above paragraph assumes the lidar

system is a direct detection configuration. Both illustrations in Figure 7 are for direct detection lidar. Figure 8 shows the same illustrations, but they are modified to become a coherent (or homodyne) detection lidar system. This design is different because it splits off a small portion of the transmit beam and redirects it towards the detector. This beam is called the local oscillator (LO). Before reaching the detector, the LO is mixed with the return signal. When these two waves of very similar frequency mix, the resulting signal is frequency downshifted to create what is called a beat frequency.

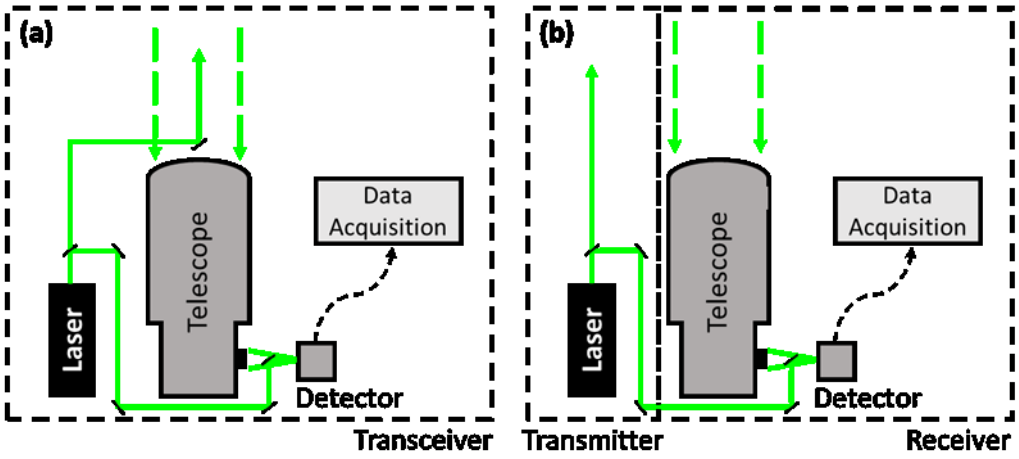

Figure 8. (a) A monostatic coherent lidar setup. (b) A bistatic coherent lidar setup.

To acquire frequency information in addition to range and light intensity information, a beat frequency is often generated. Measuring the frequency of a returning signal through direct detection is difficult to do because the frequency is extremely high. For example, green light with a 532 nm wavelength has a frequency of about 564 THz. To meet the Nyquist criterion, a device with double this bandwidth, a bandwidth of about 1.28 PHz is required. Rather than trying to build a device that can achieve these speeds, it is much easier to create a beat frequency with a LO. The resulting beat frequency is in the

kHz or MHz region, speeds that are easily achievable with current technology. For this reason, coherent lidar is more frequently used for wind lidar velocimetry.

1.4 Lidar Applications

Using lidar to measure return signal intensity, ranges, and frequency, this technology has a wide array of applications. These applications are generally broken down into two major categories: the study of hard bodies and soft bodies. The study of hard bodies relies on surface scattering of solid objects. Lidar is frequently used to perform surface mapping of solid bodies such as the part of a city in Figure 9(a). [20] A much newer application of this surface mapping technology is shown in Figure 9(b) – use in driverless cars as a scanning device to build spatial awareness while maneuvering. [21] Surface mapping is also being used by farmers on drones and tractors to help monitor the health of crops. [22] [23] In the military, scanning technology is used for identifying targets such as tanks and aircraft. [24]

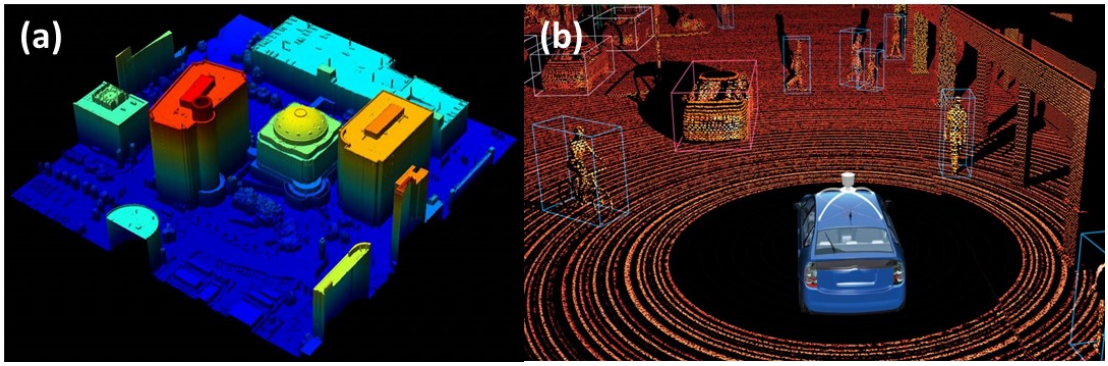

Figure 9. (a) Using lidar for surface mapping of a city. (b) Using lidar for navigation of driverless vehicles. [20] [21]

The range measuring capabilities of lidar is useful for tracking moving objects other than car speeds. For example, it is often used on satellites and other spacecraft to measure altitude changes over time, a capability useful for landing in locations such as the moon. [25] Laser Doppler vibrometry of solid bodies can be performed using range measurements at a high repetition rate or by measuring the Doppler effect caused by the motion. [26] For example, a lidar system directed at a car can measure the revolution speed of the engine via the vibrations it causes. [11]

When studying soft bodies such as clouds, lidar relies on volume scattering from molecules and aerosols. The two types of volume scattering are Rayleigh Scattering and Mie scattering, illustrated below in Figure 10. [27] Rayleigh scattering involves particles smaller than the wavelength of interest. This includes air molecules and is the reason why the sky is blue. Rayleigh scattering causes light to travel in every direction, somewhat evenly. Mie scattering on the other hand is scattering caused by particles approximately the same size of the wavelength of interest or larger. These particles include dust and other large aerosols that can be found in the atmosphere. When Mie scattering occurs, most of the scattered light continues in the direction of the incident light. The intensity of light backscattered towards a lidar system depends on the light wavelength and the types of particles in the air.

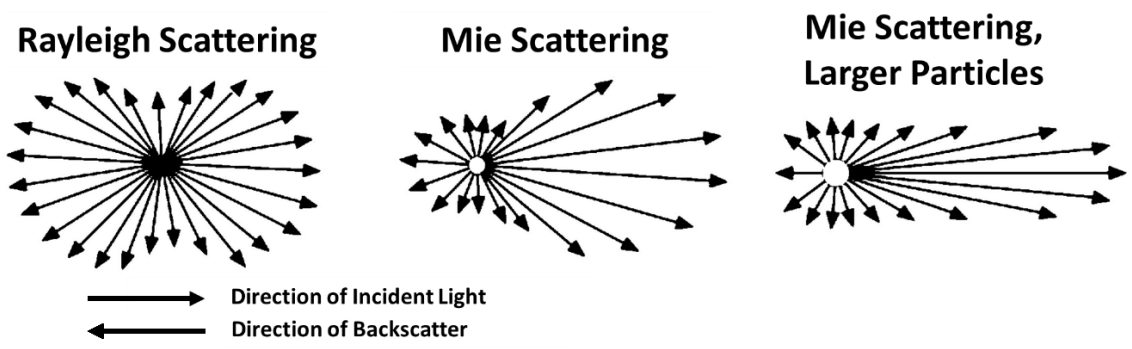

Figure 10. Mie scattering is caused by large particles while Rayleigh scattering is mainly caused by molecules. [27]

For example, when studying clouds, most of the return light is caused by Mie scattering from water vapor. Figure 11 shows results of a lidar system pointed upwards into the sky. [17] There is minor return power at most altitudes except where the clouds are located at heights of 10 and 13 km. These large particles in the atmosphere reflect much more light than air molecules, so they are easier to measure with a low power laser. The relative change in reflection intensity with decreasing particle size is shown in Figure 12. [28] The experiment performed to generate Figure 11 allowed researchers to collect information about the height, movement, and composition of the clouds. Other than clouds, this information can be gathered for measuring pollution or contaminants due to disasters such as volcanos erupting. [29]

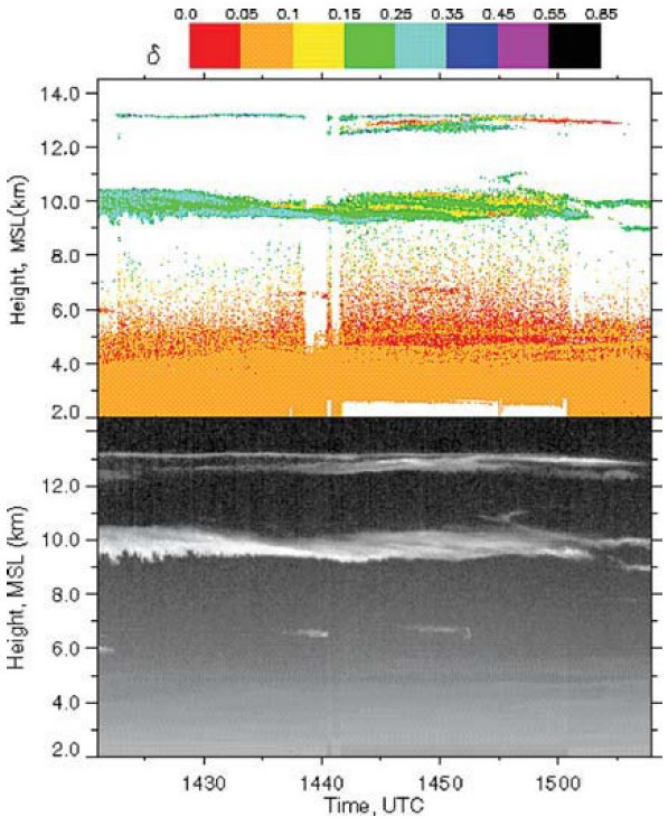

Figure 11. Lidar can be used to study cloud height, movement, and composition. [17]

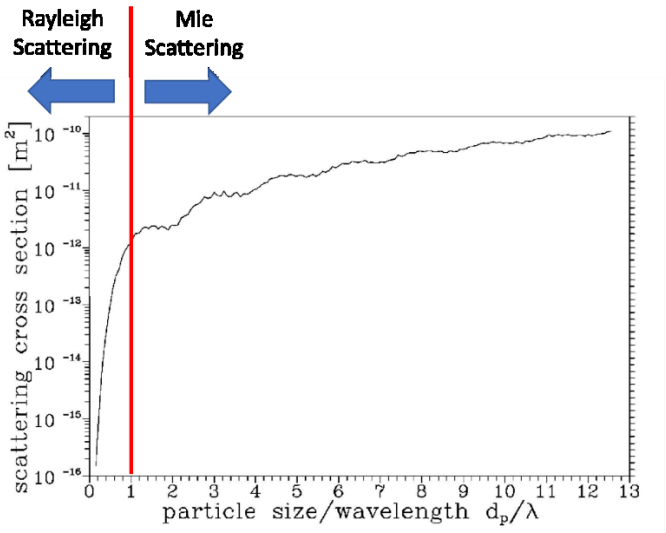

Figure 12. A much smaller return signal is received when relying on Rayleigh scattering. (Adapted from [28])

When measuring the movement of clouds, these measurements are frequently taken at a range of 2-50+ kilometers. One short range (10-200+ meters) application of velocimetry measurements include air monitoring in the vicinity of airports. [30] [31] [32] When aircraft crash while landing or taking off, it is frequently due to wingtip vortices generated by previous aircraft or wind shear hazards that include microbursts. Wingtip vortices need time to dissipate, but airports want to let aircraft take off in close succession to maximize airport capacity. Lidar systems can be used to detect both wingtip vortices and wind shear by measuring the Doppler shift associated with moving air molecules and aerosols. [33] Multiple lidar systems are commercially sold for use with this application and others. [34] [35] [36] One of these systems, the Leosphere WindCube, is shown below in Figure 13. [35]

Figure 13. The Leosphere WindCube can measure air velocities up to 200 meters above the ground. *[35]*

The same measurement technique is also applied to research for flow around wind turbines. [37] The image in Figure 14 shows results of a WindScanner Doppler wind lidar

system measuring the radial wind speed over terrain behind a wind turbine. [38] Air flow in front of and behind a wind turbine is complex and requires measuring flow velocities over a large area, including high in the air where it is difficult to reach with Pitot static tubes, hot wire anemometers, and other devices. A wind lidar system is extremely useful for making these measurements off the ground, whether for studying a current wind farm or planning turbine placements of a future wind farm. Measurement of wake steering control is useful for determining optimal placements of wind turbines in a wind farm. [39] A common lidar system used for wind turbine measurements is the ZX TM lidar system by ZX lidars (formerly ZephIR lidar). [40] Mounted on the wind turbine, it can scan at multiple ranges in front of the turbine. Figure 15 shows one of the ZephIR lidars mounted onto a wind turbine in 2017 for velocity measurements. [41] Other research conducted with a set of three WindScanner devices demonstrated the capability of three-dimensional velocity measurements around a wind turbine. [42]

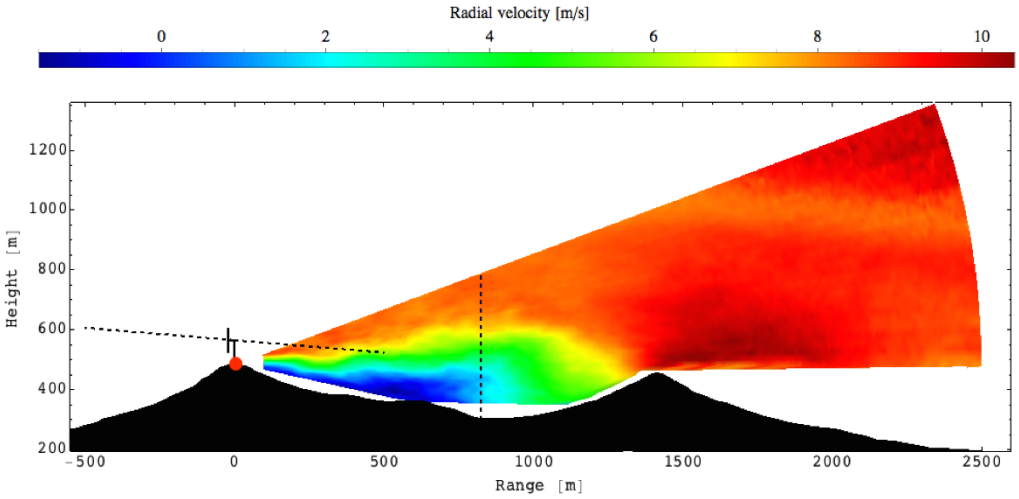

Figure 14. Lidar used to measure flow movement over terrain. (Adapted from [38])

Figure 15. The IRP Wind ScanFlow project used a ZephIR lidar for velocity measurements. *[41]*

Similar Doppler wind lidar systems have been mounted to aircraft to either point downwards towards the Earth or horizontally. One hazard in flight which is hard to determine by any means other than lidar is clear air turbulence (CAT). Statistics on the causes of airliner accidents shows that half of all accidents are caused by turbulence [43]. Changing weather and topography are what cause turbulence during flight. The CAT usually occurs at higher altitudes and cannot be detected by radar but it can be detected by airborne Doppler wind lidar with an observation range of 100-200 m. [44] Longer range lidar systems have also been studied to provide additional warning to pilots for improving reaction times. [45] Additionally, these aircraft are sometimes studied from the ground using lidar. Studying the wake of aircraft flying overhead with lidar can be used as an identification technique because each type of aircraft has a unique wake profile. [46] [47] [48]

Scientists previously investigated the use of commercial Doppler wind lidar systems in wind tunnels. A modified lidar system from ZX Lidars was used to measure one-dimensional freestream velocities inside Denmark Technical University's (DTU) wind tunnel as shown in Figure 16. [49] Lidar measurements closely matched velocities measured by a Pitot tube and pressure sensors at multiple speeds. Notice that the Pitot tube results in Figure 16 are much more scattered than the lidar and pressure sensor results. At low speeds, the stagnation pressure (upon which the device relies for measurements) is comparatively small. Low pressures lead to a low output signal strength for the Pitot tube. Just like with lidar systems, weak signals measured by Pitot tubes will lead to uncertainties.

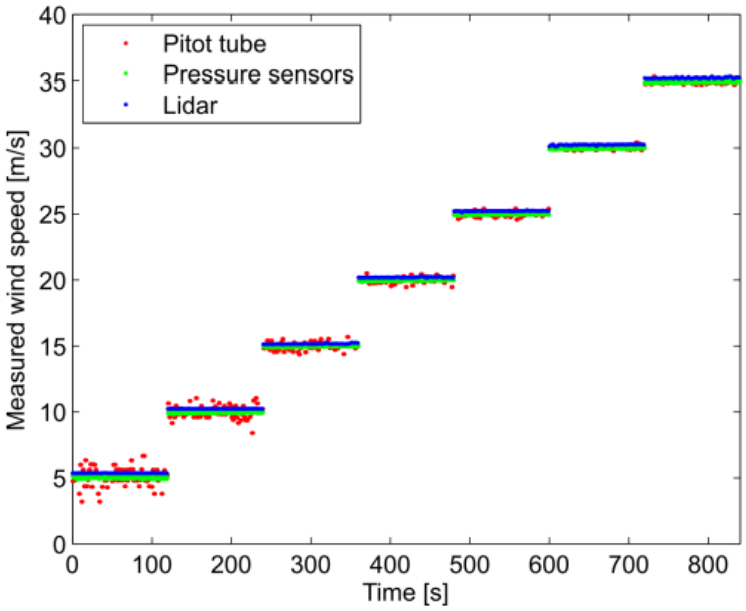

Figure 16. Wind lidar capable of one-dimensional, short range velocity measurements. (Adapted from [49])

In Italy, researchers used two modified WindScanner lidar systems to perform dual scanning of the flow, allowing them to create accurate two-dimensional flowfields around sets of scale wind turbines in a wind tunnel. [50] The illustration in Figure 17(a)

shows the two lidar systems (R2D2 and R2D3) placed near the wind tunnel walls and scanning back and forth across the wind tunnel at multiple distances downstream. Figure 18 shows a picture of one of these systems, located far away from the experiment to ensure its large wake did not interfere with the experiment. [50] The normalized flow velocity results of this experiment shown in Figure 17(b) closely matched hot wire anemometer measurements.

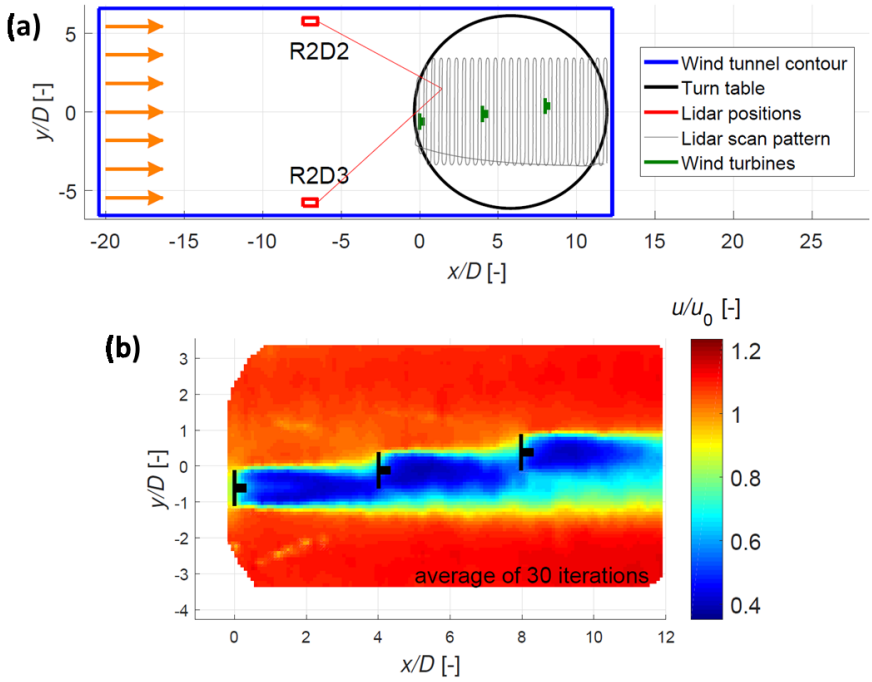

Figure 17. (a) The experimental setup for the wind lidar measurements. (b) Two-dimensional velocity measurements made by the lidar system. (Adapted from [50])

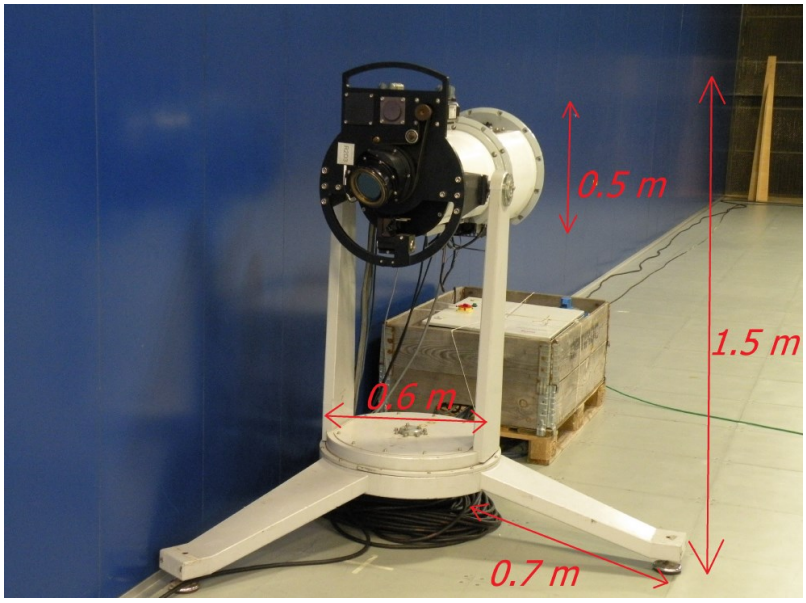

Figure 18. The lidar system is located next to the wall to avoid interfering with the experiment. *[50]*

The problem with these two experiments is their use of Doppler lidar equipment not designed for wind tunnel use. When unmodified, both pieces of equipment can measure air speeds at ranges no less than 10 meters, a distance too great for most wind tunnels. Additionally, most commercial wind lidars like the ones in Figure 13, Figure 15, and Figure 18 are over a meter tall and easily weigh at least 50 kg. Unless working in a very large wind tunnel, these devices cannot be located within the test section. The lidar system at DTU had to be modified so that the entire system was located outside the wind tunnel except for fiber optics that travelled to a transceiver device mounted inside the flow.

A system designed specifically to measure at very short ranges (such as 1-4 meters) in wind tunnels can be made smaller, require less power, and cost less than current commercial devices. Additionally, a lidar design for wind tunnels will provide an attractive alternative to current velocimetry techniques because it is nonintrusive, does not require seeding the flow, and can use a simpler setup than PIV and LDV while still providing

accurate results at high speeds if a strong signal can be measured to ensure a low uncertainty. Design and testing the first iteration of a lidar system for this purpose will be the focus in the following sections of this thesis. Once a process is developed for successfully making short range velocity measurements with lidar in a wind tunnel, future work can improve on the process.

CHAPTER II

THEORY OF LIDAR

2.1 Measuring the Line of Sight Velocity

When the laser beam of a Doppler wind lidar travels down range into moving air, it may not always be travelling parallel to the streamlines. A single lidar system measures one component of the flow velocity along the laser beam, V_{LOS} which is defined as

$$V_{LOS} = V_{\infty} cos(\theta) \tag{7}$$

where θ is the angle between the laser and the fluid velocity. Relying on the frequency information that can be gathered using lidar, the shift in frequency can be used to calculate V_{LOS}. The beat frequency, f_{beat}, between the LO frequency, f_{Laser}, and the return signal, f_{sig} shifted by Δf (the Doppler shift) is calculated as

$$f_{beat} = \left| f_{sig} - f_{Laser} \right| = \left| f_{Laser} + \Delta f - f_{Laser} \right| = \Delta f \tag{8}$$

The shift in frequency of the return signal is caused by the movement of the reflecting air molecules and aerosols in relationship to the lidar system. This frequency shift measured by the lidar system, explained by the Doppler effect, is related to the measured velocity by

$$\Delta f = \frac{2V_{LOS}}{\lambda} \tag{9}$$

This equation is rearranged to solve for velocity.

$$V_{LOS} = \frac{\lambda \Delta f}{2} \tag{10}$$

By measuring the Doppler shift of light waves reflecting off moving air molecules and aerosols in a wind tunnel, the line of sight velocity can be determined. A positive Doppler shift represents air moving towards the lidar system while a negative shift represents air

moving away. Equation 10 also gives an idea about the uncertainty associated with the velocity measurement using Lidar. As previously mentioned, these Doppler shifts are in the kHz or MHz region. If the Doppler shift can be known to an uncertainty of 10 kHz, the corresponding velocity uncertainty is on the order of 0.01 m/s. To detect the Doppler shift, the photodetector must be sensitive enough and laser strong enough for a measurable return. If this return is weak and hard to distinguish from noise, the uncertainty will quickly rise.

2.2 Estimating Lidar Return Power

Calculations to determine the required output power are based on the number of photons required by a photodetector for detection. The energy in each travelling photon (E_λ) is given by

$$E_\lambda = \frac{hc}{\lambda} \tag{11}$$

where h is Planck's constant. The number of photons output from the laser (N_0) during a photodetector integration time, τ, is

$$N_0 = \frac{P_0}{E_\lambda}\tau \tag{12}$$

Where P_0 is the laser output power. Substituting equation 11 into equation 12,

$$N_0 = \frac{P_0\lambda}{hc}\tau \tag{13}$$

The number of photons reflected backwards towards the collector lens depends on N_0, the probe length Γ, Rayleigh cross-section per unit volume β_m, and the collector lens frontal area A. The probe length is given by

$$\Gamma = \frac{\lambda R^2}{\pi w_0^2} \tag{14}$$

where λ is the wavelength of light, R is the measurement distance and w_0 is the laser's beam waist. The Rayleigh cross-section per unit volume is given by [51]

$$\beta_m = 1.39\left(\frac{550}{\lambda(nm)}\right)^4 X\ 10^{-12} \tag{15}$$

Equations (13-15) are inserted into the equation below to estimate the number of photons returning to the collector lens (N). [52]

$$N = \frac{3}{16\pi\Gamma^2} N_0 c A \beta_m \tag{16}$$

When measuring at extremely short ranges inside of a wind tunnel, atmospheric attenuation is assumed to be negligible, so this value is left out of equation 16. While the number of photons output by the laser during the integration time of interest is in the billions, the number of return photons can easily be in the hundreds or fewer.

When increasing the wind tunnel speed or moving to a higher speed wind tunnel such as the vertical wind tunnel at the Air Force Research Laboratory (AFRL) inside Wright Patterson Air Force Base (WPAFB), the photodetector bandwidth requirement increases. When the bandwidth increases, the reduced integration time means fewer photons are captured by the photodetector within one integration time period. In summary, higher wind tunnel speeds demand faster photodetectors which lead to a lower measured return signal intensity. When the return signal is weak, the theoretically low lidar uncertainty is likely to increase. To ensure a low enough uncertainty is achieved to match PIV and LDV, a strong signal intensity is needed. Lower wind tunnel speeds allow for use

of slower equipment, and higher signal strengths can be achieved with the lower bandwidth to minimize uncertainty.

2.3 Lidar Component Descriptions

2.3.1 Photodetectors

Details of the two main components of a lidar system, the light generating laser and the light measuring photodetector, are discussed here. The number of return photons calculated for a given lidar design, as described in Section 2.2, must be high enough for a photodetector to capture at its operating bandwidth. A photodetector collects return photons and converts them into current output by the diode. The photodetector used in a Doppler wind lidar setup controls the return signal intensity requirement and velocity measurement limitations. The three main types of photodetectors used in lidar are PIN diode detectors, linear mode avalanche photodetectors, and Geiger mode avalanche photodetectors. Understanding how each type of photodetector works is helpful in deciding which to use when designing a lidar system and calculating the number of return photons. The general construction of a photodiode is shown in Figure 19 below. [53] The two main components of a photodetector are the P-region (positive region) and N-region (negative region), semiconductors grown through diffusion on P-type and N-type substrates, respectively. The location where these regions meet is called the P-N junction. Originally, the N-region has a negative charge because it has many free electrons while the P-region has a positive charge because it has many free positively charged holes. When the two regions are put together and meet at the P-N junction, the holes and electrons diffuse to the

opposite side. The P-type end of the diode ends up being the anode while the N-type end of the diode ends up being the cathode.

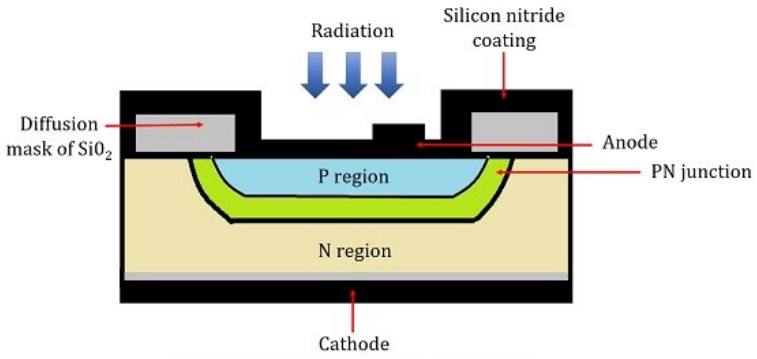

Figure 19. Major components of a photodiode inside a photodetector. [53]

The image in Figure 20 illustrates how a photodiode operates. [54] A voltage is applied to the diode which causes a slight amount of current, called dark current, to flow through the photodiode whether or not light is impacting it. The breakdown voltage is the minimum voltage that must be applied to make the diode become conductive. With a voltage applied to the device, electrons throughout the diode move away from the P-region, pushed by the negative power source terminal. Similarly, holes throughout the diode move away from the N-region, pushed by the positive terminal of the power source. The movement of electrons and holes creates positively and negatively charged ions that combine at the P-N junction in an area called the depletion region where an electric field is generated. This configuration is called a reverse bias voltage. As the reverse bias voltage is increased, the depletion region grows because electrons and holes are drawn more strongly towards the positive and negative terminals, respectively. Increasing the reverse

bias voltage increases device sensitivity but also increases dark current (which creates noise).

When exposed to light, photons enter the depletion region. This added energy causes the holes and electrons to separate. Free electrons are then drawn towards the power source's positive terminal while holes are drawn towards the power source's negative terminal, creating additional current flow. The greater the intensity of light, the greater the number of electrons/holes separated which leads to more current output. The relation between incident light intensity and output current is linear.

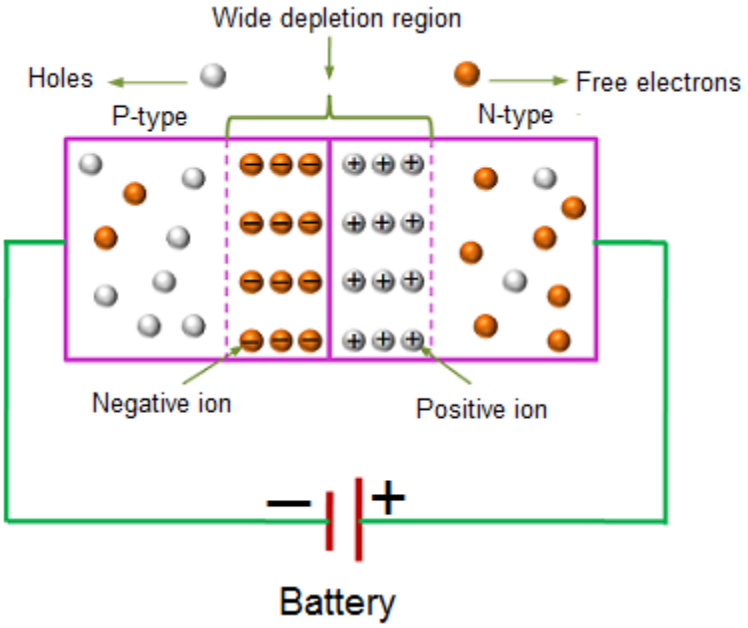

Figure 20. Movement of electrons in a photodiode creates current. [54]

PIN photodiodes also include an intrinsic region between the N-region and P-region that creates high resistance between the anode and cathode. This allows for a high reverse breakdown voltage and therefore larger depletion regions. The I-region causes the P- and N-regions to separate more which leads to a higher frequency response. A higher

frequency response is helpful for improving the velocity ranges a lidar system can measure. Linear mode avalanche photodetectors (APDs) increase sensitivity over PIN photodetectors using a gain mechanism. The electric field in the diode is made stronger through an increased reverse bias voltage. When photons separate pairs of electrons/holes, they experience high acceleration due to the strong electric field. The electrons and holes impact other pairs and cause additional pairs to become separated (an avalanche). This leads to a stronger output signal from the device and allows users to detect lower light levels than PIN detectors. A lower return light intensity requirement allows for measurements at longer ranges and higher detection speeds.

Another type of photodetector is the Geiger mode avalanche photodetector. While linear mode detectors operate below the breakdown voltage, Geiger mode detectors operate above the breakdown voltage. Operating above the breakdown voltage causes a strong avalanche of electrons to occur when a photon impacts the surface. Only one photon is required to trigger avalanches in a Geiger mode detector. The number of electrons output by a Geiger mode detector is the same for each time it is triggered compared to linear mode detectors that have an output that varies linearly with the received signal intensity. After a Geiger mode detector is triggered, the bias voltage is reduced to below the breakdown voltage level to quench the detector and stop current flow. While this process occurs, the detector cannot be triggered by another photon. The time it takes for a Geiger mode detector to quench before it is ready to accept another photon is known as the dead time. The dead time for these detectors can be upwards of 1 μsec before the bias voltage is increased again. [11] This can be problematic for high speed applications such as Doppler wind velocimetry that require bandwidths greater than 1 MHz. Recently, Geiger mode arrays were introduced

that can provide asynchronous readout, but this technology is still very new and expensive. [11]

The use of Geiger mode detectors is becoming more popular for other lidar applications. For example, Geiger mode detectors are useful for mapping terrain because it is easier to see through foliage than other photodetectors. It performs better with foliage because only one photon needs to pass through the foliage and back whereas other detectors need many photons to successfully pass through the foliage for a readable signal. This increased sensitivity also allows for mapping to be performed at longer ranges which means areas can be scanned faster. Detecting single photons can be problematic for Doppler wind lidar inside of a wind tunnel because any ambient light in the room will cause the detector to trigger. Using a narrow band interference filter can help this problem to an extent. [55] In addition to ambient light in a wind tunnel, researchers would also need to deal with laser line of sight issues. If light from the laser reflects off any surface, it can create additional false triggers that contribute to background noise. This complication cannot be solved with a filter because it is the same wavelength of light being collected.

As previously discussed, these photodetectors need to capture photons reflected backward due to volumetric scattering. When avoiding the use of tracer particles only Rayleigh scattering contributes to the total backscatter. The very weak expected backscatter strength is what makes wind lidar extremely difficult to perform. While a wind lidar system can be simplified for use in wind tunnels compared to measurements at long ranges, measuring the return signal remains a challenge. Unless the system is sensitive enough, the return signal is lost in noise added when the photodetector is converting the light waves to an electrical signal.

2.3.2 Photodetector Noise

Several common types of noise are dark noise, cross talk, and shot noise. The first type of noise, dark current noise, occurs independent of the incident photons. When a photodetector is operating but not receiving any light, a small amount of current, called dark current, continues to pass through the device and generate noise. Simulation of dark current is shown in Figure 21 below. [53] Any reverse bias voltage applied to a detector will create dark current. As the incident light intensity increases, the reverse current increases to levels much greater than the dark current, at which point the noise generated by dark current is negligible. If photodetectors are mounted in an array, a second type of noise that is generated is cross talk. When using a detector array, the electrons released by a single detector can turn into photons and be released inside of the detector housing. This will cause other detectors to fire and generate noise in the form of false signals.

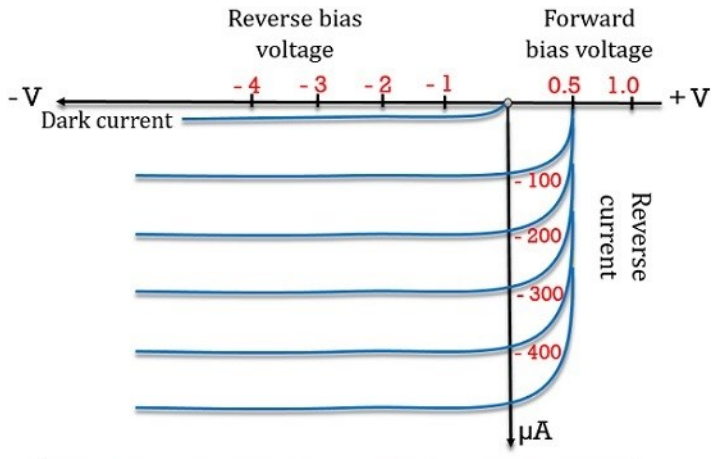

Figure 21. Dark noise is present whether or not a photodetector is receiving light. [53]

The final major type of noise output by photodetectors is called shot noise. Shot noise is defined by the random, slight variations in the number of electrons emitted from a photodetector over time. The random arrival of photons to the photodetector is the source of shot noise, and it has a Poisson distribution. [56] Shot noise increases with light intensity, but not as fast as the overall output signal. [11] If the output signal is strong, the ratio of shot noise to signal is small. The intensity of light scattered by air molecules is small which means the return signal of Doppler wind lidar is weak. When working with weak signals, the fluctuation in electrons will have a much higher relative effect. Using a LO in coherent detection lidar, the total light intensity received by the detector is greater. This increased signal causes shot noise to be the dominant noise source. [11] Additionally, using a strong LO improves the signal to noise ratio (SNR). The electric signal intensity output by a photodetector for coherent detection is

$$I = 2E_{sig}E_{LO}\ e^{-j(\omega_{sig}-\omega_{LO})} \tag{6}$$

Where E_{sig} and E_{LO} are the electric fields caused by the return signal and LO, respectively; ω_{sig} and ω_{LO} are the spatial frequencies of the return signal and LO, respectively. [11] When the return signal is weak, there can still be a strong photodetector output signal at the beat frequency if the LO intensity is strong.

2.3.3 Lasers

The proper choice of a photodetector in a lidar system is strongly dependent upon the laser (light amplification by stimulated emission of radiation) in use. For example, the measured return signal power (and therefore required detector sensitivity) is directly related to the laser power output. An illustration of a typical laser's interior is shown below in

Figure 22. [57] A pump source adds energy to a lasing medium, stimulating the electrons inside. The stimulated electrons move from a ground state to an excited state at an outer ring of the atoms inside the lasing medium. The electrons, after a brief moment in this excited state, move back down to their ground state and emit photons in the process. Constant pumping of the lasing medium causes photons to be continuously released by the electrons. Two parallel mirrors located at each end of the lasing medium reflect the photons back and forth while the light inside amplifies over time. One mirror is partially reflective which allows light to exit the optical resonator as a beam.

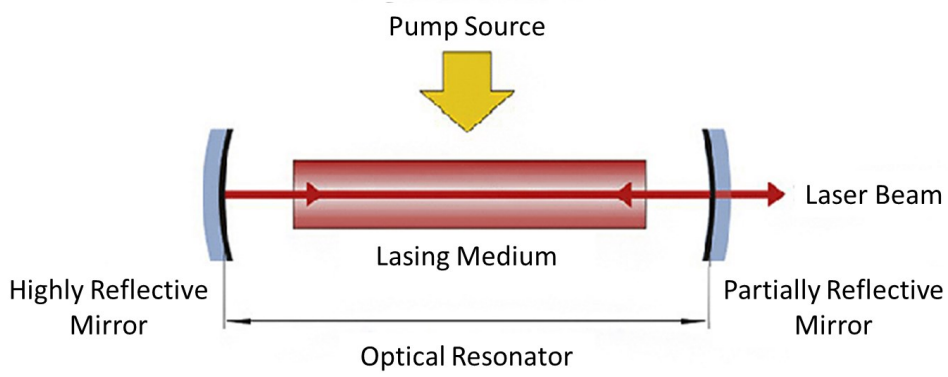

Figure 22. Photons are released by pumping energy into a lasing medium. *[57]*

Lasers can be either pulsed or continuous wave (CW) with slightly different interior constructions. Both types of lasers are used in lidar systems, but CW lasers are more popular for wind lidar. A pulsed laser emits light from the laser in short bursts that are of high intensity. These bursts can last several nanoseconds, but various lasers have different ranges of pulse widths. CW lasers on the other hand emit one continuous beam of light, but they do not have the same power capabilities as pulsed lasers.

When selecting a laser for use in lidar, several considerations must be made. One laser specification to consider is the coherence length. Each photon in one pulse of a pulsed laser may have a slightly different wavelength, but they are close enough in frequency to still constructively interfere when overlapped. The distance the laser pulse can travel before the photons inside the pulse no longer constructively interfere is the coherence length. As mentioned previously, a coherent detection lidar system must mix light from the LO and return signal that both originate from the same outgoing pulse (if using a pulsed laser) to ensure the wavelength is consistent. Unless the LO pulse of a pulsed laser is delayed until the signal pulse returns, the laser's coherence length must match the total travel distance of the signal pulse. [11] A laser specification related to coherence length is the laser linewidth. Laser linewidth is the range of wavelengths possible from a laser. The pulses of a pulsed laser will all be slightly different. A CW laser will have a changing wavelength with time. Inconsistencies in the wavelength can contribute to the uncertainty of a Doppler lidar system. It is best to select a laser with a very narrow linewidth when designing for wind lidar.

Another consideration, the laser power, is a direct driver of the return signal strength and must be accurately estimated in advance when designing a lidar system. Additionally, the laser wavelength must be selected. The laser wavelength controls what material is used for the lasing medium. For Doppler lidar, the wavelength controls the Doppler shift magnitude per equation (9). High wavelengths (such as in the infrared spectrum) lead to a Doppler shift in the kHz region while shorter wavelengths (such as in the visible or ultraviolet spectrum) lead to a Doppler shift in the MHz region. As seen in equation (15), the wavelength is also a driver of the Rayleigh scattering strength. This is

extremely important because the wind lidar system designed for this research is expected to rely on Rayleigh scattering alone for a return signal. The return signal strength changes with the inverse of wavelength to the fourth power. Maximizing the return power of a lidar system requires low wavelengths when working with Rayleigh scattering.

Equations and equipment information presented in this chapter are what drive the design selections for a lidar system. Each of these sections are relied on for the discussion in the next chapter when designing the lidar system for construction. The design includes selection of required equipment specifications and how best to arrange the equipment for measurements of the Doppler shift.

CHAPTER III

LIDAR DESIGN

3.1 Lidar Preliminary Design

Two designs were considered when deciding how to construct a Doppler wind lidar system. Both designs relied on coherent detection to measure the Doppler shift. A schematic of the first design is shown below in Figure 23. This monostatic design relied on the polarization of light to separate and merge the LO and signal beams at the beamsplitter. A variable half wave plate at the laser made the beam linearly polarized. The wave plate would be adjusted so that almost all power is transmitted down range to reflect off air molecules. Two lenses expand and focus the outgoing beam to a point down range where the velocity is measured. The reflected return signal travels the same path back and is condensed to a beam again. Quarter wave plates make the beam circularly polarized when travelling through the LO and down range but converts it back to a linear polarization for merging again at the beamsplitter. After merging the LO and return signal at the beamsplitter, the resulting signal with a beat frequency travels towards the photodetector (PD) for measurement and analysis. Initial work with this design showed that it was difficult to ensure minimal power was used in the LO to not damage the photodetector and maximize the return signal. Additionally, the return signal and LO would have different linear polarizations. When the light waves are not oscillating in the same direction, they are not spatially matched and therefore were expected to not mix well for generating a strong beat frequency.

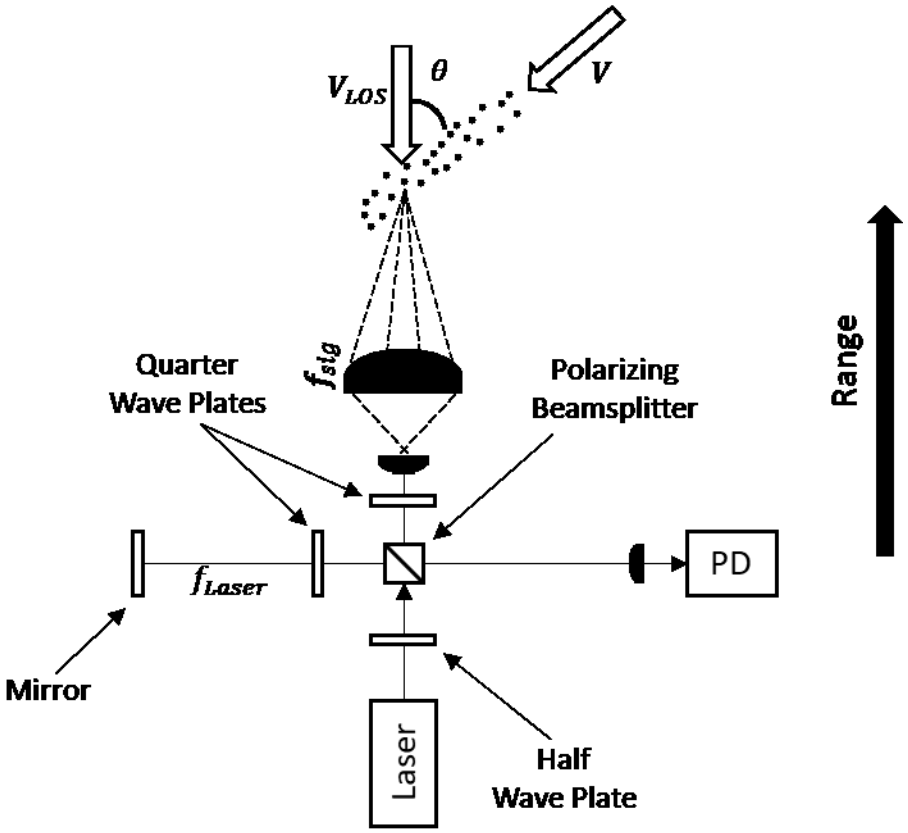

Figure 23. The first design considered relied on polarization to split and recombine beams.

The second coherent lidar system considered (and the design ultimately selected) uses a bistatic setup and is shown in Figure 24. After light exits the laser, it passes through a 90:10 unpolarized beamsplitter cube to redirect 90% of the laser power down range into the flow where it reflects off air molecules and aerosols. A beam dump (BD) is positioned down range of the measurement region to capture the beam and prevent reflections from contributing to the output noise of the photodetector. The reflected light is collected by a large plano-convex lens positioned to be directed towards the beam. The light passing through this lens is focused and collimated by a secondary, smaller (4mm diameter) plano-convex lens. These lenses were sized and positioned to make the return signal beam comparable in size with the LO beam.

At the same time, the other 10% of the light split at the beamsplitter passed through a reflective filter (RF) to lower the LO power. The power was reduced to a level that would not damage the photodetector. After passing through the RF, the LO and return signal were combined at a secondary 90:10 beamsplitter cube. After combining the beams, the light passes through a final condenser lens that focuses the light onto the active area of the PD. The PD then measures the beat frequency between the LO and the return signal.

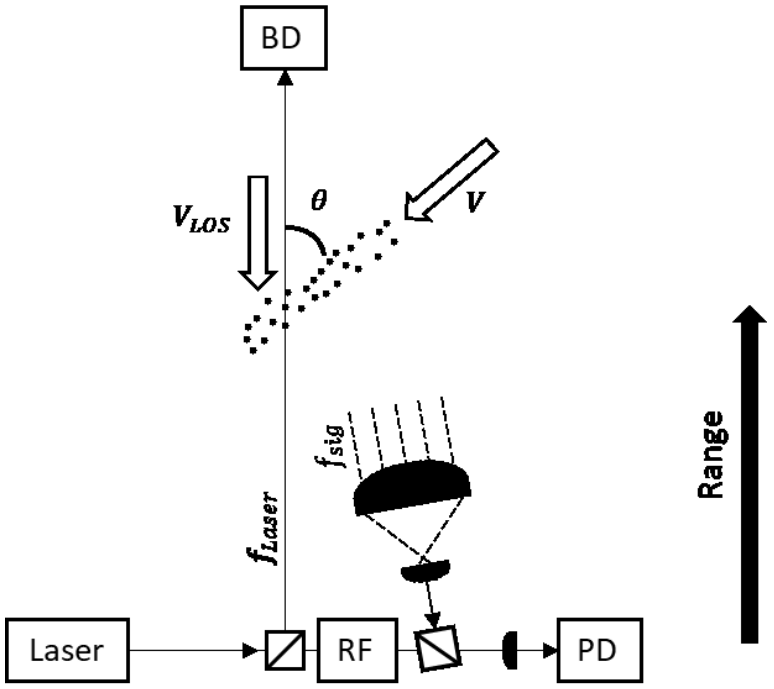

Figure 24. The basic components for coherent detection Doppler wind lidar used in the final design.

The laser beam travelling down range experiences Rayleigh scattering from all air along the beam, not just at the range of interest. If all reflected light was measured by the photodetector, the lidar system would not have a useful range resolution. With this design, only light that passes through the collector lens is condensed onto the PD and can be measured. At the selected measurement range of 1.5 meters (to be discussed later), a 10 cm

section of the beam properly passes through the optical train and is captured by the photodetector. This means that the system measures all velocities within this 10 cm section of the beam. If the flow velocity is constant throughout the beam, only one speed is measured. If the flow is accelerating through here, multiple velocities are measured because multiple Doppler shifts of varying magnitudes are occurring.

3.2 Lidar Detailed Design

Multiple items were considered when selecting a laser for the Doppler wind lidar system including measurement distances, velocity measurement range capabilities desired, safety, and setup of the system. The Doppler shift decreases with an increase in wavelength which allows for lower bandwidth photodetectors to be used. On the other hand, Rayleigh scattering decreases with wavelength to the fourth power, so shorter wavelengths were preferred to improve what is already a weak return signal. [58] A 532 nm wavelength laser was selected for the lidar system partly because optical equipment is easy to acquire at this wavelength. Additionally, this is in the visible spectrum, so setting up equipment is easier and safer than higher or lower wavelengths.

When operating at this wavelength, the Doppler shift is 3.76 MHz per every 1 m/s. The University of Dayton low speed wind tunnel (UD-LSWT) can operate at speeds from 1-37 m/s which has an associated Doppler shift range of 3.76-139.1 MHz. The photodetector (to be discussed later) must meet the Nyquist criterion to capture all Doppler shifts possible, so it must have a bandwidth of at least 278.2 MHz. To maximize the strength of the return signal, the laser pulse length must be the length of the photodetector integration time or longer. Making the pulse length at least twice the photodetector

integration time ensures that the photodetector is collecting as much light as possible for a stronger signal. Doing this causes time periods of little to no power measured by the photodetector between pulses, effectively reducing the bandwidth of the detector. To simplify the system, a CW laser was selected to continuously provide the photodetector with light.

A sensitivity study was performed on several inputs to equation (16) to help select optimal operating conditions for the lidar system. Figure 25 shows the variation in the number of return photons as a function of wind tunnel velocity (and therefore required detector integration time) and laser power. The velocity range goes up to 50 m/s, the highest achievable velocity of the vertical wind tunnel at AFRL. The horizontal axis on the top of the plot shows the Doppler shifts associated with these velocities. A measurement range of 1.5 m and return collector diameter of 150 mm was assumed in this analysis. A typical PIN diode photodetector can detect as few as 400 incident photons during an integration time period. For a linear mode APD, this lower limit is closer to 50 photons. Finally, Geiger mode detectors require only several photons for an output. Red lines in Figure 25 shows the operation limits of PIN diode and linear mode APD.

Since Geiger mode APDs are much more expensive than other types of photodetectors and have limited options for achieving high bandwidths, this type of photodetector was avoided, limiting testing conditions and ranges. PIN diode detectors could only measure speeds up to about 25 m/s with even a 500 mW laser. Linear mode APDs are more sensitive without too much of a price increase, so the system was designed to work with a linear mode APD. The minimum power required for a linear mode APD is 150 mW. The selected laser power of 200 mW is 33% greater than the minimum to help

account for inefficiencies and any other losses that could occur in the lidar system. A Cobolt Samba™ CW laser operating at a 532 nm wavelength and 200 mW was selected for experimentation. [59]

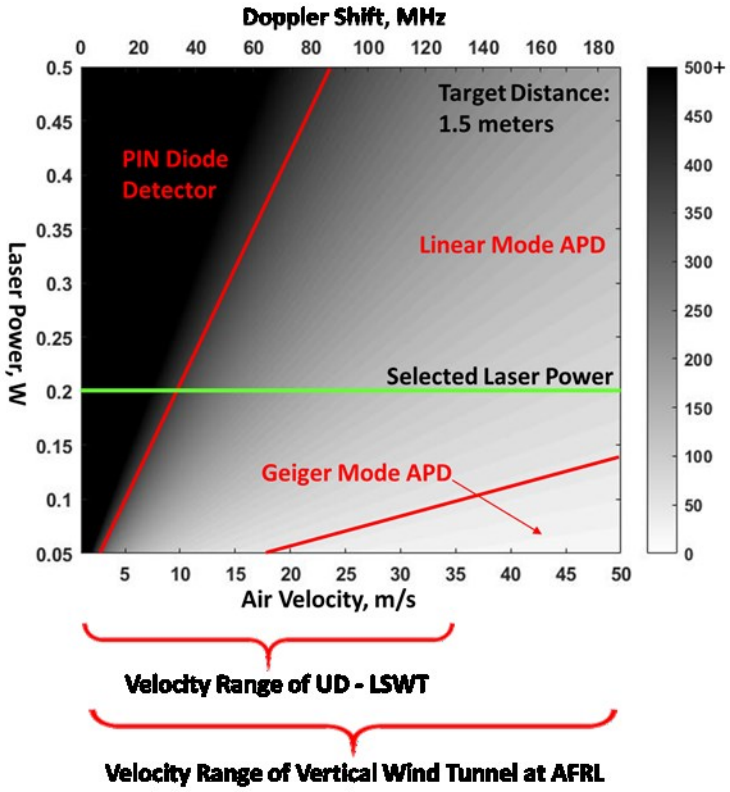

Figure 25. The number of return photons for a given laser power indirectly varies with air velocity.

The same analysis procedure was repeated with a 200 mW laser and a varying measurement distance because the number of returning photons decreases with range to the fourth power. The measurement distance could not exceed 1.75 m to operate with a linear mode APD at all wind tunnel velocities of interest. Additionally, limited options exist for commercially available plano-convex collector lenses with a larger diameter that could extend this limit. Ultimately, a 1.5 m measurement distance was selected.

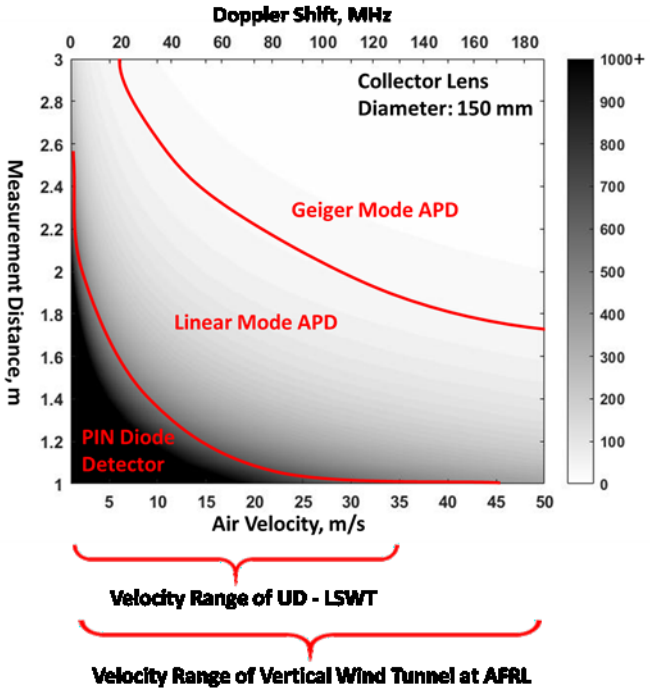

Figure 26. The number of returning photons decreases with the square of measurement distance.

Ultimately, a Silicon linear mode APD was selected from Thorlabs (APD 430A2) that was designed to operate in the visible spectrum and has a bandwidth of 400 MHz. [60] Based on the above calculations, the APD 430A2 was expected to be sensitive enough to detect the return signal at all velocities of interest. Additionally, the bandwidth is high enough for measurement speeds up to about 53 m/s – high enough for the UD-LSWT and AFRL vertical wind tunnel. The responsivity plot of this APD is shown below in Figure 27 where the 532 nm operating wavelength is shown with a vertical bar. The detector is UV compensated to improve the responsivity at 532 nm. Additionally, a variable gain from 10 to 100 allows for flexibility while testing. Once the photodetector and laser were selected, more detailed design of the lidar system was performed to select the proper optics

for controlling the beam throughout the optical train in the experimental setup described in the next chapter.

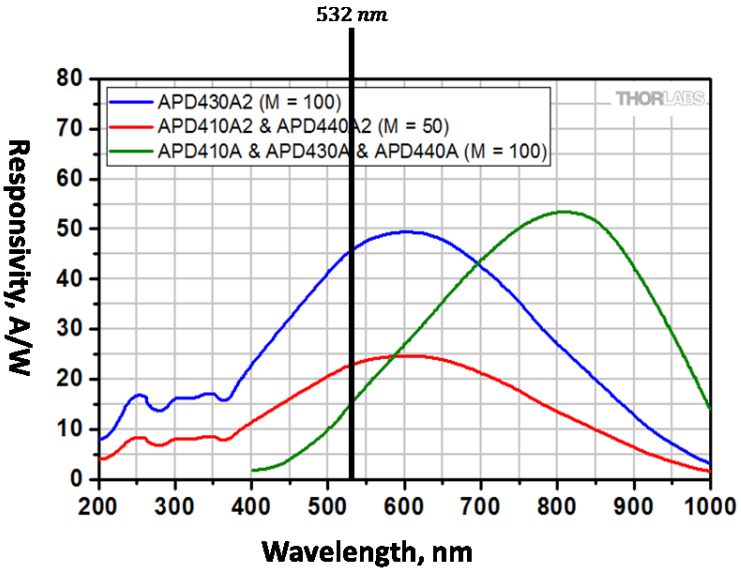

Figure 27. Responsivity curves of the selected APD (APD430A2) and several similar devices. (Adapted from [60])

CHAPTER IV

EXPERIMENTAL SETUP

4.1 Equipment Setup

The equipment described in the previous chapter was purchased and set up at the Ladar and Optical Communications Institute (LOCI) at the University of Dayton. The equipment used in the experiment is listed in Table 1. The image in Figure 28 shows what the lidar system looks like, mounted onto an optical table. The outgoing beam travels down range to pass through the 1.5 m measurement point where the collector lens is pointed. The APD is connected to an InfiniiVision DSO-X 3012A oscilloscope that can operate up to 100 MHz. Despite having a 400 MHz APD, the oscilloscope bandwidth in this setup is the leading constraint in what speeds can be measured (up to 13.3 m/s).

Table 1. Equipment Specifications of the constructed Doppler wind lidar design.

Equipment	Manufacturer	Specifications
Photodetector (APD430A2)	Thorlabs	200-1,000 nm, 400 MHz, Silicon, variable gain
Laser (Cobolt Samba)	Cobolt AB	CW, 532 nm, 200 mW
Filters	Thorlabs	Reflective, Variable Optical Density
Beamsplitters	Thorlabs	90:10 (R:T), non-polarizing, 400-700 nm
Collector Lens	Edmund Optics	150 mm diam., 200 mm focal length
Focusing Lens	Edmund Optics	4 mm diam., 4 mm focal length

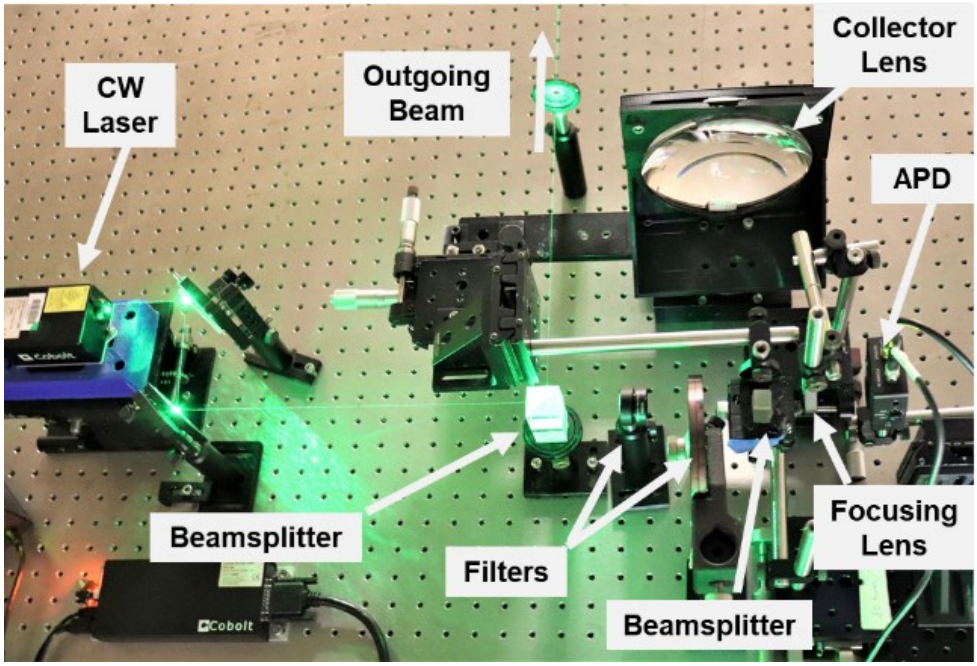

Figure 28. The designed lidar system constructed for testing at LOCI.

To fine-tune alignment of the system, necessary equipment was mounted to optical linear stages. The ten one-axis stages allowed for precision motion control, down to thousandths of an inch. Extremely fine motion control was critical because the LO and return signal light beams need to be parallel and mixing when reaching the APD. The collector lens was located on a rotary stage which allowed the system to turn for collecting light from different distances down range. The collimating 4 mm lens was then rigidly attached to the collector lens to minimize the amount of adjustments that need to be made when measuring at different ranges.

Finally, the beamsplitter cube used to merge the LO and return signal was mounted onto a rotating kinematic table platform. This additional control helped to ensure the two beams were coaxial with each other after exiting the beamsplitter and travelling towards the APD. As a bistatic system, the return light does not travel perpendicular to the outgoing

beam. When studying objects at long ranges, as frequently done with other lidar applications, a bistatic system is easier to align because it is safe to assume that the light captured by the collector lens or telescope is travelling parallel to the outgoing beam. At short ranges, this angle is exacerbated (to approximately 5.7°) to the point that the assumption can no longer be made. The beamsplitter cube was rotated to ensure the return signal was coaxial with the LO.

To ensure the LO and collected returning light were condensed and overlapping at the photodetector during alignment, a 2.3 MP FLIR Grasshopper3 CMOS camera (Model GS3-UC-23S6M-C) was put in place of the APD. [61] The camera has a 1920 x 1200 resolution with 5.86 μm pixel size. With variable exposure time, the camera can achieve frame rates up to about 190 fps. This is well short of the speed required for detecting the beat frequency, so it could only be used to determine proper mixing and overall alignment. Figure 29 below shows several images captured with the FLIR camera. Parts (a) and (b) show representative images of the captured light from the return signal and LO, respectively. In part (a), the outer ring is created by the edge of the 4mm lens while most light is concentrated in the center. Spherical aberration causes the light to not focus to a single point in space, so the diameter of the light beam at the focus point can only be concentrated to a limit. Ideally, the two light sources are focused to a perfect point at the same location on the APD. Part (c) of the figure shows what it looks like when the two light sources are not aligned. The optical system must be adjusted with the traverses until they overlap like shown in Figure 29(d). In this image, the fringe patterns caused by the two signals interfering constructively and destructively are visible. The outside of a ring of

fringe patterns is shown with a dotted line. The stronger the fringes, the stronger the beat frequency signal measured by the APD.

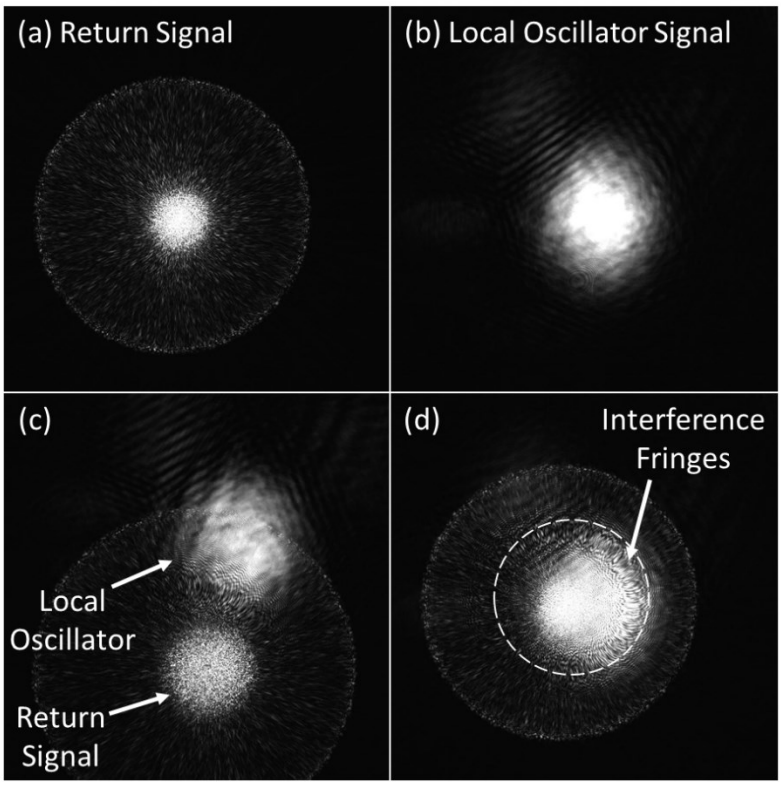

Figure 29. Fine tuning the system alignment to ensure the LO and return signal beams properly overlap.

In Figure 30 below, part (a) shows a zoomed in version of Figure 29(d) above where the fringe patterns are shown more clearly. Part (b) of the figure below shows an improvement in the focusing of the optical system to make the return signal concentrated onto a smaller dot. The entire light area behind this dot in part (b) is the LO kept at a large size rather than focusing it to be a comparable diameter to the return signal. While the large size LO was not used for final testing, it was expanded using a 5X beam expander to make initial beam alignment easier. The blue circle in these images represents the size of the

APD sensor. The APD is only able to capture a fraction of the light gathered by the collector lens. The APD covers only about 10% of the return signal area in part (b) of the figure. Assuming the light intensity is equally distributed across this area (which it is not), that would mean only 10% of the return power is captured by the APD. When focused properly, a large portion of the return signal light is concentrated in the center of the dot, so the APD is capturing more than 10% of the return power even though it is only covering 10% of the area.

Another important item to note regarding Figure 30 is that the APD captures multiple light fringes across its active area. The number of fringes incident on the APDs active area varies from 5 to 15 fringes. A high spatial frequency of these fringes lowers the mixing efficiency of the two beams. Mixing efficiency is directly proportional to the intensity of the APD output signal. [11] As an analogy, it is easy to tell when a room is dark if there is only one light turning on and off. If instead there are multiple lights in the room turning on and off at different times, there is never a clear moment of bright and dark. This is what the APD is experiencing during all testing. If one fringe covered the entire APD's active area, there would be a very clear frequency at which the signal intensity increased and decreased. This frequency could be measured with a greater mixing efficiency and therefore require a lower power laser. Spatially adjusting the mixing of the two light sources alters the fringe pattern and therefore the mixing efficiency.

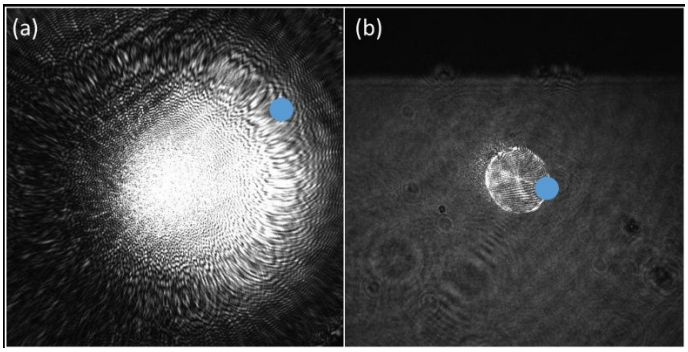

Figure 30. The blue dot represents how much of the return light hits the photodetector.

4.2 Test Procedure

Preliminary testing was performed on the LIDAR system to ensure the optics are aligned and can detect a Doppler shift. At the 1.5 m measurement range, a piezoelectric ultrasonic transducer was mounted and set to vibrate at 1.44 MHz. [62] This transducer was selected because it could create a measurable frequency with a similar magnitude of that expected for the Doppler shift in a wind tunnel. In this configuration, the system performs as a vibrometer rather than a Doppler wind lidar. If the LO and return signal are properly aligned, the system should detect a beat frequency that matches the vibration frequency of the transducer. Using a transducer first is beneficial because it causes surface scattering rather than volume scattering caused by air and generates a much stronger return signal that can easily be measured by the APD for initial testing. With this strong signal, fine tuning of the lidar system was performed to properly align all the components and maximize the APD output signal.

After the system was tested to measure vibrations of a hard body target, the transducer was replaced with a small-scale wind tunnel to determine its capabilities for measuring the Doppler shift generated by moving air in the inlet and test section of a wind tunnel. A schematic of the 3D printed small-scale wind tunnel is shown in Figure 31. The

lidar system was oriented to measure spatial acceleration inside the wind tunnel collector. The 10 cm measurement region previously discussed was located between points A and B in the figure. Point C represents the center of a second test measurement region that focuses on flow inside the test section rather than accelerating flow inside the inlet. Testing was performed inside the scale wind tunnel with and without tracer particles added to the flow. To seed the flow, a steam generator was used to blow water vapor into the air in front of the inlet. The steam generator can be seen seeding the flow in Figure 32. The tracer particles had an estimated diameter of 10 μm which has a Stokes number of 0.090 for 9 m/s flow. [63] The tracer particles follow the fluid flow to an acceptable level since the Stokes number is much less than unity. [64] The tracer particles caused Mie scattering to occur in addition to Rayleigh scattering, and the return signal power was increased. This difference is noticeable in Figure 32 – the beam looks much brighter once it enters the region containing tracer particles.

To validate lidar velocity measurements, a Pitot static tube (with an uncertainty of 0.1 m/s) was mounted inside the wind tunnel at points A, B, and C. The measurements taken by the Pitot static tube at two slightly different speed settings are shown in Figure 31. When measuring acceleration, the lidar system should detect Doppler frequencies associated with all velocities between points A and B for a given wind tunnel setting. When focused inside the test section, the lidar system should measure a consistent velocity because flow does not accelerate inside the test section.

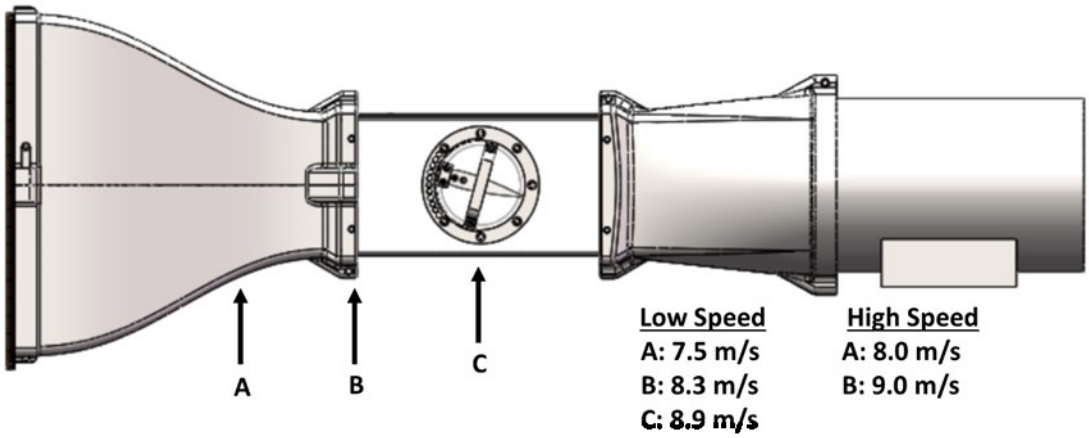

Figure 31. Low and high speed measurements were taken with a Pitot static tube.

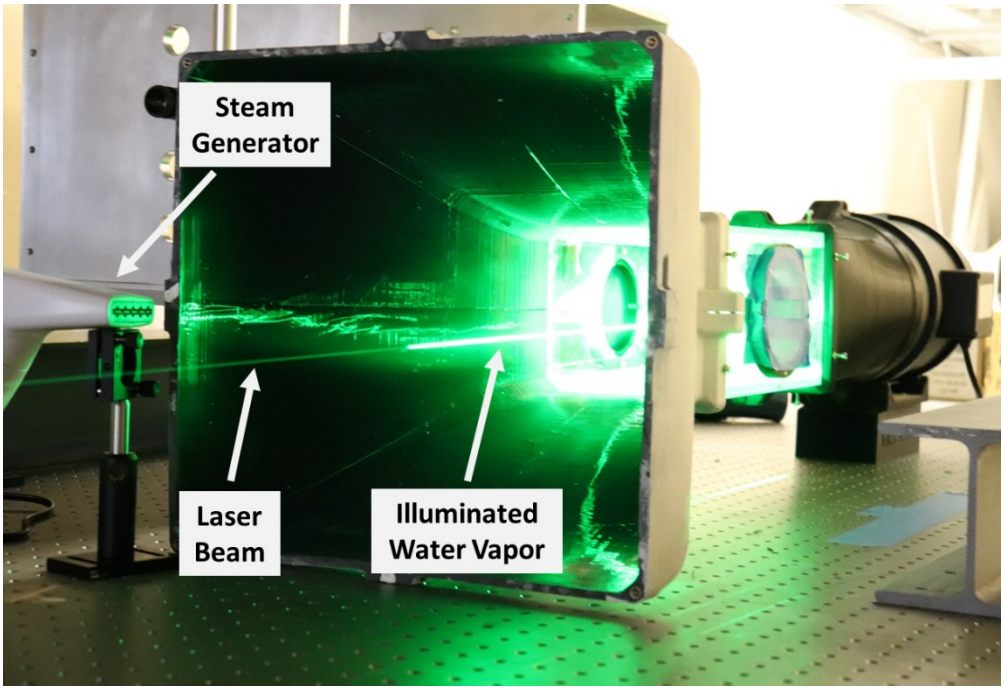

Figure 32. The steam generator causes a much greater return signal inside the wind tunnel.

4.3 Data Analysis

The APD's output to the oscilloscope, upon exposure to the mixture of return signal and LO, is in the form of voltage over time rather than a frequency. The voltage data was collected over a 200 μs time period with a sampling rate of 80 MHz resulting in 16000 data

points. The resulting frequency resolution (sample rate divided by number of data points) is 5 kHz which has an associated velocity resolution of 0.0013 m/s for a 532 nm wavelength. For the speeds generated by the wind tunnel, the oscilloscope was set to collect data at 80 MHz rather than 100 MHz since the Doppler shift was not expected to go beyond 40 MHz. To determine the beat frequency of the APD output signal (and therefore the Doppler shift value needed for a velocity calculation), a Fourier transform was performed to convert it into the frequency domain. The general Fourier transform equation for a two-dimensional function is [65]

$$F(g) = \iint_{-\infty}^{\infty} g(x,y) \exp[-2\pi j(f_X x + f_Y y)]\, dxdy \tag{17}$$

The above equation can be simplified to a one-dimensional integral with respect to time [66]

$$F(\omega) = \int_{-\infty}^{\infty} f(t) \exp[-j\omega t]\, dt \tag{18}$$

To perform this computation numerically, a discrete Fourier transform (DFT) is performed [66]

$$X_k = \frac{1}{N} \sum_{r=0}^{N-1} v_r \exp\left[-i\left(\frac{2\pi kr}{N}\right)\right] \tag{19}$$

where N is the number of data points in a dataset (16,000 in this case), v_r is the voltage sequence of the dataset, and $k = 0, 1, 2 \ldots (N-1)$. When analyzing the voltage sequence output by the oscilloscope, Matlab was utilized to perform the DFT using a fast Fourier transform (FFT) algorithm. [67] After performing the FFT, the resulting vector was raised to the sixth power to help make signal peaks more visible in plots. For the wind tunnel test, the low speed Pitot static tube velocity measurements should correspond to an associated Doppler shift of 28.2 and 31.2 MHz, so peaks in the FFT data were expected in this range.

At least 200 datasets were gathered for each wind tunnel velocity to help account for the expected weak signal strength. While the APD noise is random (white), the signal was expected to be repeatable within the expected frequency ranges.

A cutoff amplitude was set in the FFT results to separate the signal from the noise. Peaks in the FFT data with magnitudes greater than the cutoff amplitude were considered "signal" while all other information in the FFT plot were considered "noise". An example of what this would look like is shown below in Figure 33. To quantify the strength of the signal in results, a SNR was defined as the ratio of the average signal peak amplitude to the cutoff amplitude. In the example below, the average signal peak amplitude is 0.92. If the cutoff amplitude was set to 0.3, the data would have a SNR value of 3.07. This process was repeated for all FFT plots to compare results.

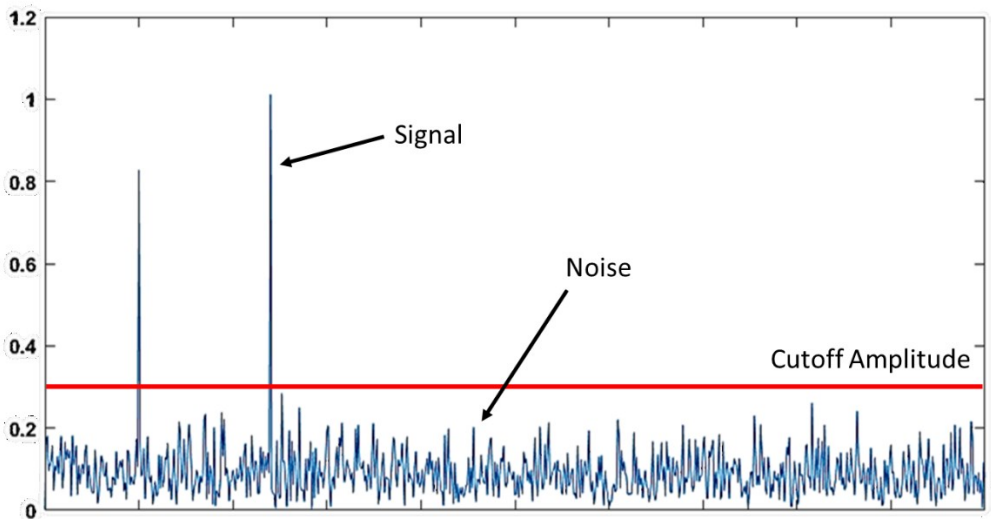

Figure 33. An example of how a cutoff amplitude is used to differentiate signal and noise.

In this chapter, the experimental setup of the lidar system was described in addition to the planned analysis of the APDs output during testing. The goal of testing

performed with this wind lidar system was to detect the Doppler shift required for making a line of sight velocity measurement. A SNR greater than unity in the test results means that the described tests are successful in measuring the Doppler shift. The next chapter contains results of the transducer and wind tunnel testing. These results are interpreted and discussed to determine how successful the designed lidar system is at measuring wind tunnel line of sight velocities.

CHAPTER V

RESULTS AND DISCUSSION

5.1 Transducer Test

Figure 34 shows results of the transducer experiment performed to test the system's capability of measuring a Doppler shift. The highly reflective surface of the transducer, shown in the image within Figure 34, generated a strong return signal that was easily measured by the APD. The plot shows the amplitudes of the return signal at various frequencies up to 40 MHz. A clear set of overlapping peaks are visible at 1.44 MHz, the input frequency to transducer. This test proves that the system is properly aligned and working as intended, at least when a strong return signal is present.

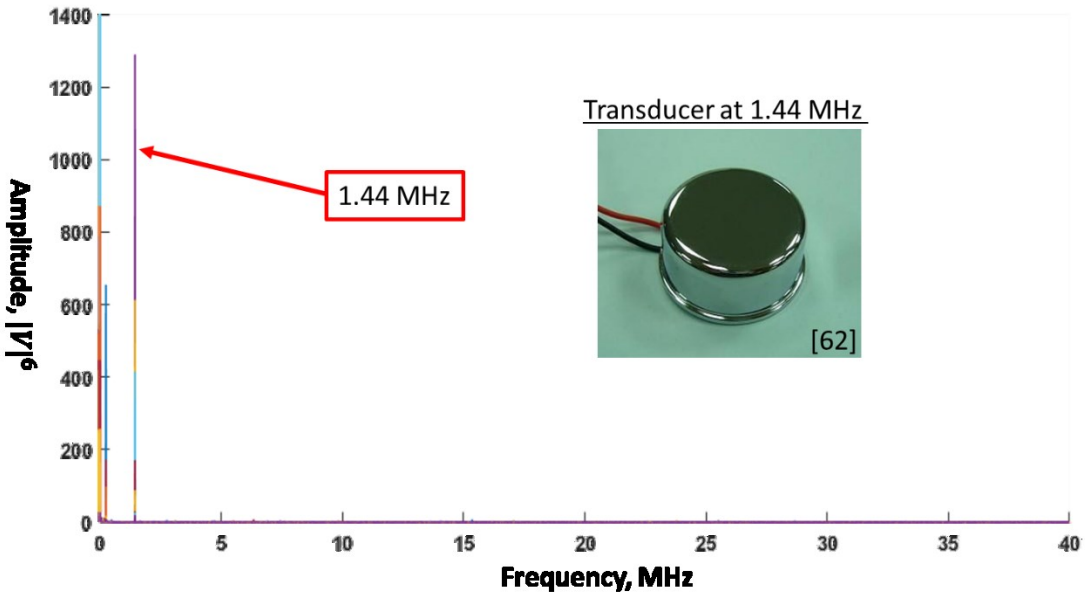

Figure 34. A transducer operating at 1.44 MHz reflects enough to be detected by the lidar system. (Inset image of transducer from [62])

A zoomed in view of the transducer results is shown below in Figure 35. Each peak in the FFT has a full width at half maximum (FWHM) of approximately 3 kHz. The frequency peak of all transducer datasets varied by no more than ± 1 kHz from the average frequency peak. This frequency uncertainty corresponds with a velocity uncertainty of ± 0.00027 m/s if measured in air. With a frequency uncertainty this low and minimal bleed over into other frequencies, there is potential here for extremely accurate velocity measurements. In addition to having potential for wind lidar being an alternative to PIV and LDV, this can potentially perform as good as hot wire anemometers for turbulence intensity measurements and other applications. That being said, these are ideal laboratory conditions with a stronger return signal than can be achieved using Rayleigh scattering alone. Wind lidar uncertainties will likely never quite be this low.

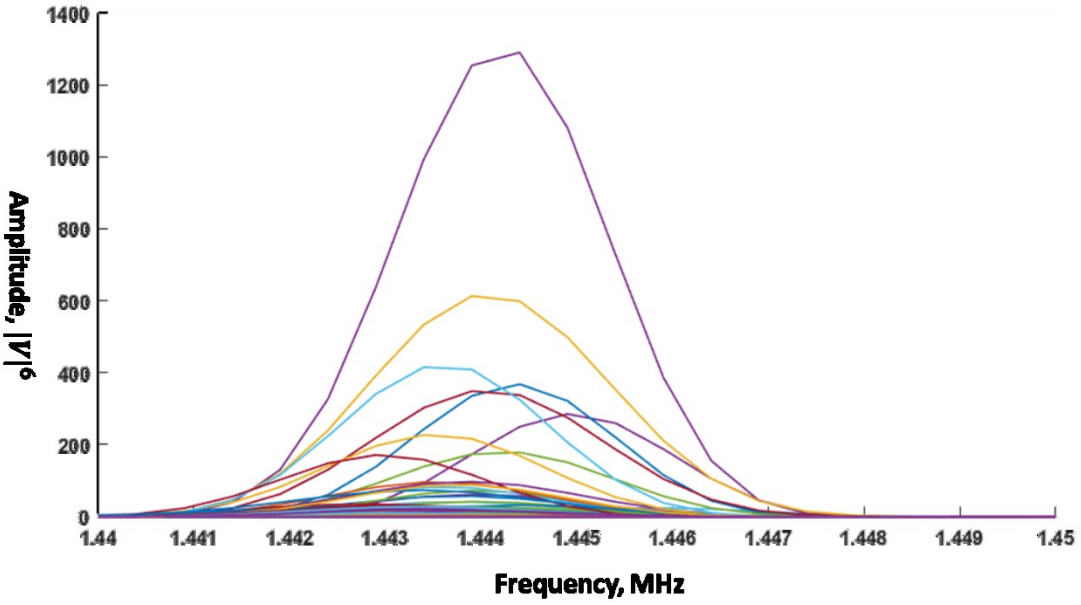

Figure 35. A zoomed in view of the ultrasonic transducer lidar results.

A comparison of Figure 35 with Figure 36 helps to show the importance of a strong LO in coherent lidar. The results plotted in Figure 36 show a test performed with the transducer where 100 datasets were collected while the LO had a much weaker signal sent to the APD. At the same y-axis scales, the peaks are almost no longer visible on the plot. A low LO intensity results in an overall low SNR. These results show in a physical sense how the LO signal strength is directly proportional to the APD signal as described in equation (6).

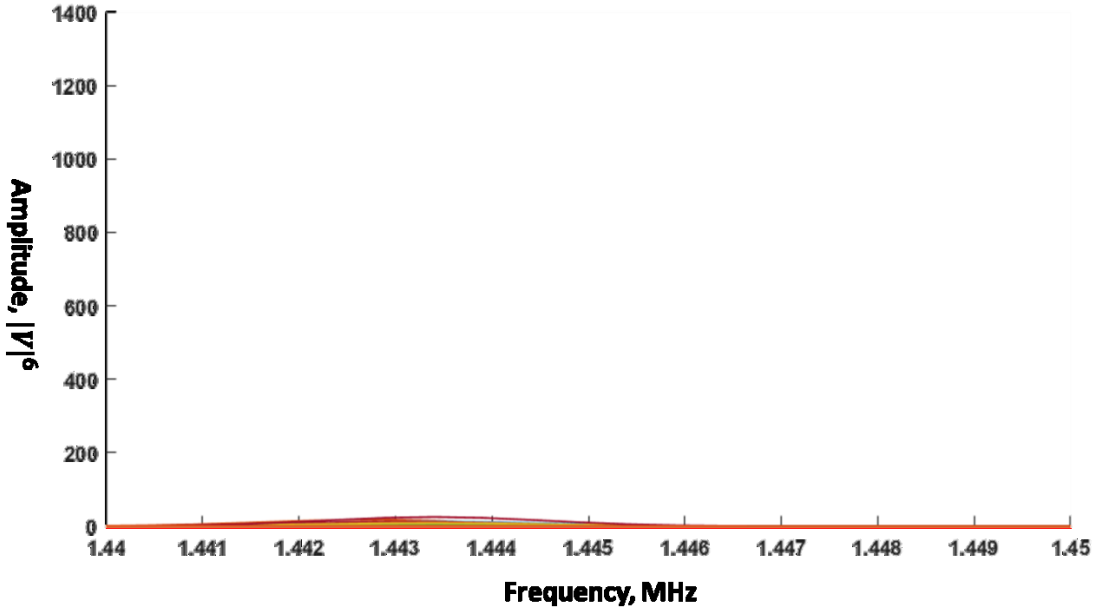

Figure 36. When the LO signal is weaker, the beat frequency is also weaker.

5.2 Wind Tunnel Tests

The next test performed was velocity measurements in the small-scale wind tunnel at the low speed setting using seeded flow. Results of this test for 200 datasets are shown in Figure 37. The two x-axes show the output frequencies of the FFT and the velocity associated with these Doppler shifts. The Pitot static tube measurements showed an

acceleration in the flow from 7.5 to 8.3 m/s between points A and B of Figure 31. Any peaks below the cutoff amplitude of 100 were not considered in the analysis. The resulting peaks in the area of interest around a frequency of 30 MHz totaled 28 from the 200 datasets with a SNR of 3.31. The size and number of peaks generated by a given dataset varied greatly with the density of water vapor in the measurement region while each dataset was collected. Most datasets did not have enough return signal to generate a beat frequency that surpassed the cutoff amplitude. Of the peaks calculated from the datasets, they all were in the range of 28.24 to 31.33 MHz which are associated with velocities of 7.51 and 8.33 m/s, respectively. The Doppler lidar measurements accurately measured the acceleration through the region of interest, varying from the Pitot static tube measurements by no more than 0.03 m/s. The difference between the lidar and Pitot static tube measurement is within the Pitot tube measurement error. A summary of the differences between lidar and Pitot static tube measurements are summarized in Table 2 after all results are displayed.

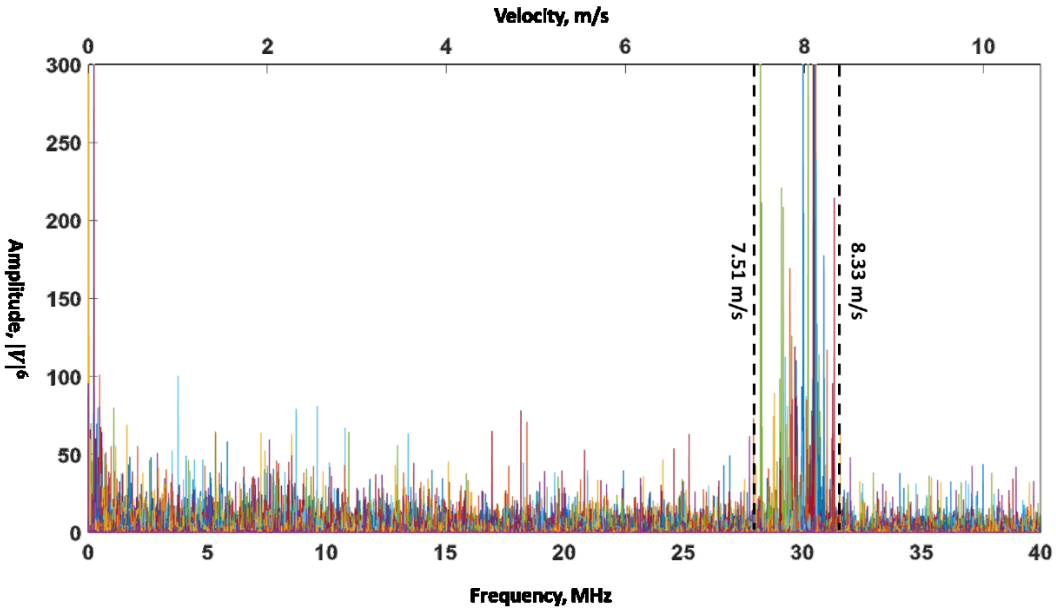

Figure 37. Results of 200 datasets from the low speed wind tunnel test using seeded flow.

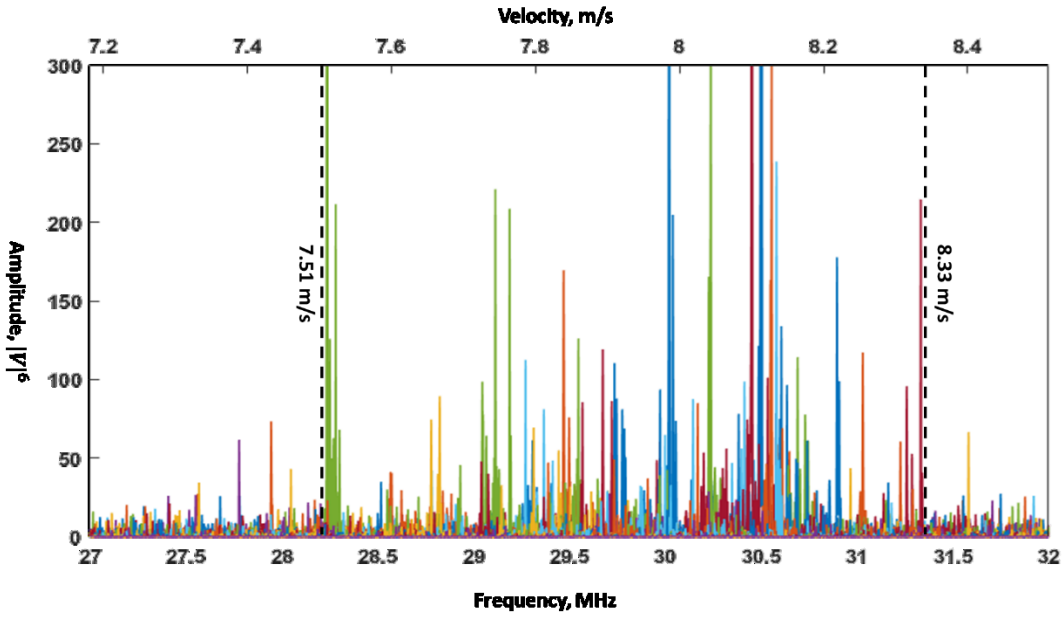

Figure 38. A zoomed in view of the low speed wind tunnel inlet results.

The scale wind tunnel fan rotation speed was increased for a second test at a higher air velocity given the relative success of the first wind tunnel test. The high speed results are shown in Figure 39 with a zoomed in view of the FFT plot shown in Figure *40*. One peak did not lie within three standard deviations (a 99.7% confidence interval) of the mean frequency and was set aside as an outlier. The other frequency peaks varied from 30.42 to 33.78 MHz which is equivalent to a velocity measurement range of 8.09 to 8.98 m/s. Once again, the lidar measurements match the Pitot static tube measurements within the Pitot static tube error values. This data has a SNR of 3.31, almost the same as with the low speed testing.

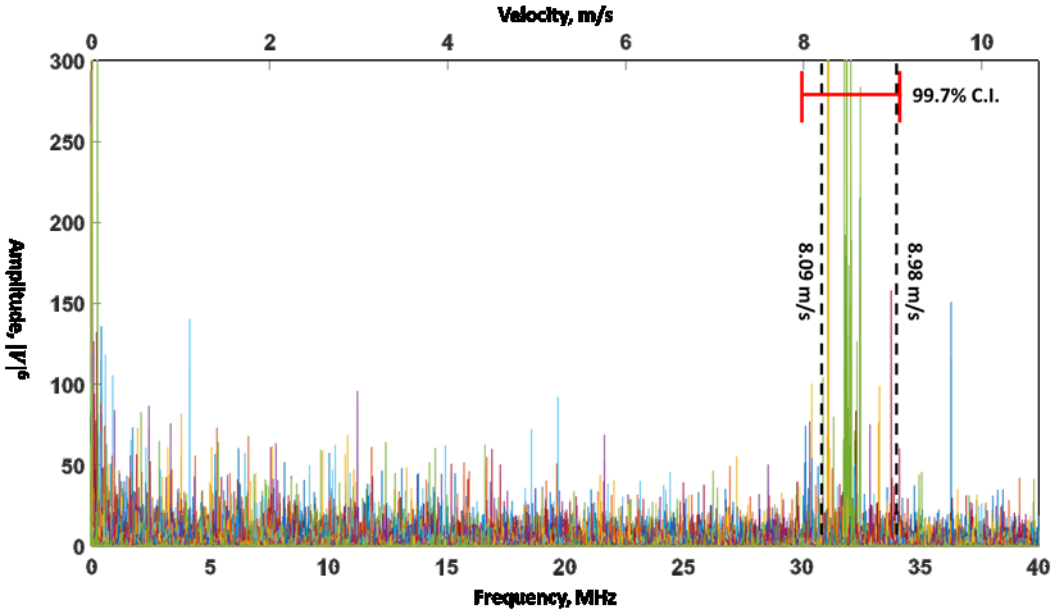

Figure 39. Results of 200 datasets from the high speed wind tunnel test using seeded flow.

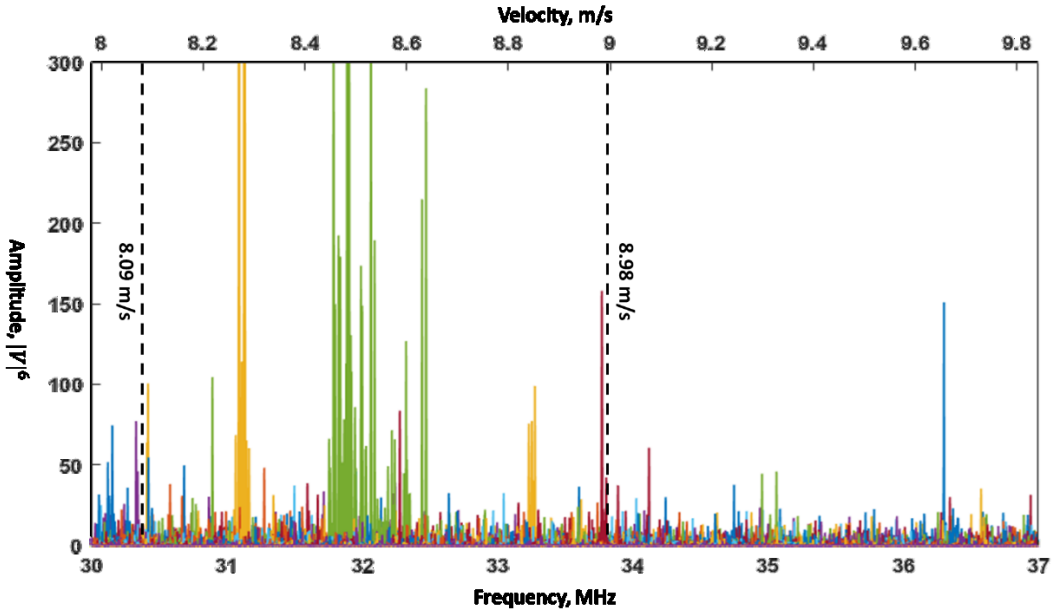

Figure 40. A zoomed in view of the high speed wind tunnel inlet results.

A total of 26 peaks were detected with an amplitude greater than 100 for the high speed test, two less than the low speed test. A breakdown of the number of peaks generated

by each dataset for the low and high speed tests is shown in Figure 41. Each point in the scatterplot represents one dataset of information collected from the oscilloscope and shows how many peaks with an amplitude greater than the cutoff resulted from each dataset. As previously discussed, most datasets generated zero peaks due to a weak signal. Despite being a similar number of peaks for the low and high speed tests, the vapor visually appeared to disperse more for the high speed test as it travelled through the inlet to the measurement region. Additionally, fewer datasets contributed to the total number of peaks for the high speed test. One of the datasets with a very strong return due to dense seeding at the time of measurement was responsible for 18 of the 26 frequency peaks in the high speed test. Finally, a large majority of the peaks originated from the second 100 datasets collected for the low and high speed tests. After the first 100 datasets were collected, a slight adjustment was made in the optical train which improved the signal strength measured by the APD. The plot in Figure 41 shows how sensitive the lidar system is to minor adjustments in alignment. If alignment is improved, fewer datasets will be required to measure velocities.

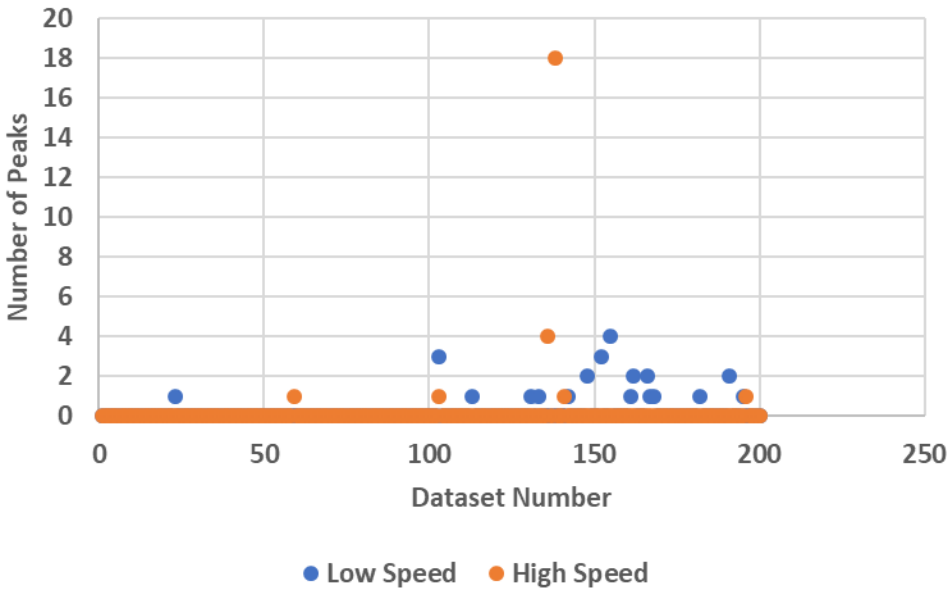

Figure 41. How peaks had an amplitude greater than 100 for each dataset of inlet testing.

In the low and high speed tests with seeded flow, one dataset ideally has frequency peaks at every velocity between points A and B in the scale wind tunnel because the lidar system is collecting light from the entire 10 cm measurement region. While a couple datasets covered a large portion of the velocity (and therefore spatial) region, most only had one peak at a single velocity. The tracer particles likely had a non-uniformity in the measurement region along the beam during the data acquisition time periods. When a non-uniformity is present, only certain parts of the beam are "visible" to the APD because too few tracer particles are present to reflect enough light to the APD from other portions of the beam.

After performing tests inside the wind tunnel inlet, the lidar system was adjusted to focus on the test section with seeded flow. Figure 42 shows results of the additional test where 200 datasets were gathered with the wind tunnel on the low speed setting. A zoomed

in view of the frequency peaks is shown in Figure 43. The 10 cm measurement range extended from approximately the entrance of the test section to the exit. The speeds measured by the Doppler wind lidar system were between 8.11 m/s and 9.68 m/s with an average peak velocity of 8.98 m/s. The average velocity varies from the Pitot static tube measurement by 0.08 m/s which is within the Pitot tube's uncertainty. At the low speed setting, the wind tunnel travels at 8.3 m/s near the exit of the inlet as measured by the Pitot static tube and lidar system (refer to Figure 37). It is possible that the flow finishes accelerating to 8.9 m/s in the back end of the inlet before it enters the test section. Ignoring the several other frequency peaks, this consistent velocity result is expected because the flow velocity should not change as it passes through the test section – the cross sectional area remains constant. Ideally, a test section velocity is perfectly constant; in reality, all wind tunnels have a small fluctuation in the velocity. The several frequency peaks not close to 8.9 m/s can potentially be caused by accelerations or decelerations at the test section inlet or outlet. The lidar system still measures all speeds within a 10 cm section, so it is capturing any minor changes in the air velocity throughout the test section. Based on the central cluster of frequency peaks in Figure 42, the wind tunnel velocity varies by $\pm 1\%$ throughout the axial length of the test section.

This set of 200 datasets has 29 frequency peaks with an amplitude greater than 100 in the frequency range of interest. The number of peaks here is slightly greater than the number of peaks detected for low and high speeds inside the inlet, and they have a much greater SNR of 8.04. Since the test section is further away from the tracer particle source (the steamer), it was expected that there would be fewer frequency peaks with lower amplitudes for this testing than the inlet testing. Finding the amplitude and number of

frequency peaks to increase for test section testing suggests that the tracer particle density throughout the flow is not consistent during testing. This matches with qualitative data visualized throughout testing.

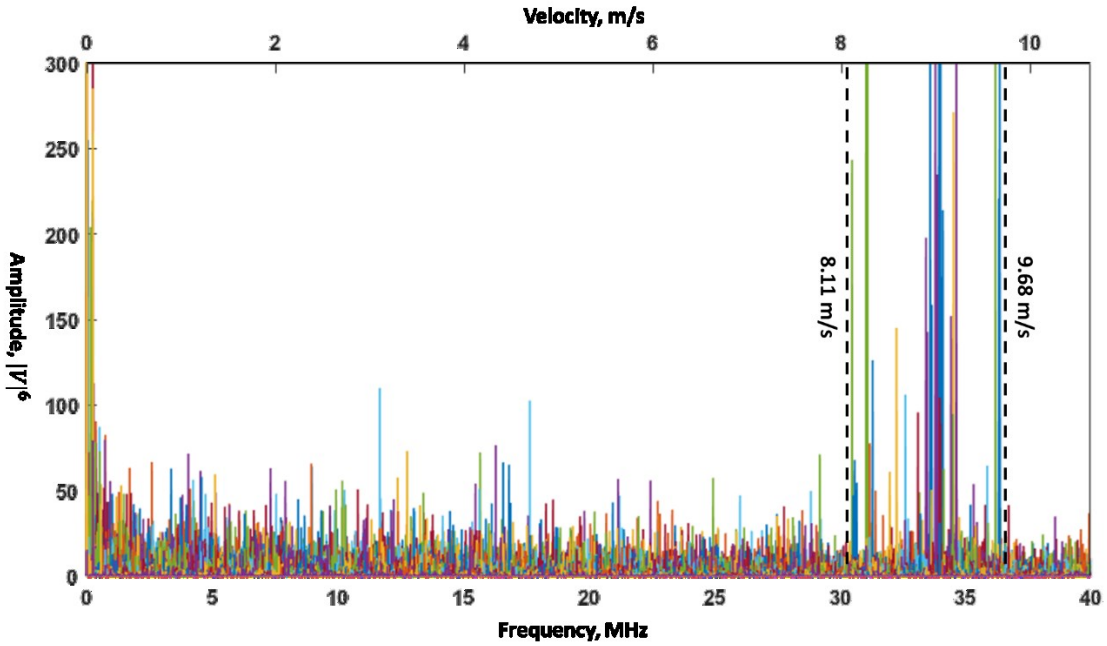

Figure 42. Results of 200 datasets with the lidar focused on the center of the test section at the low speed setting.

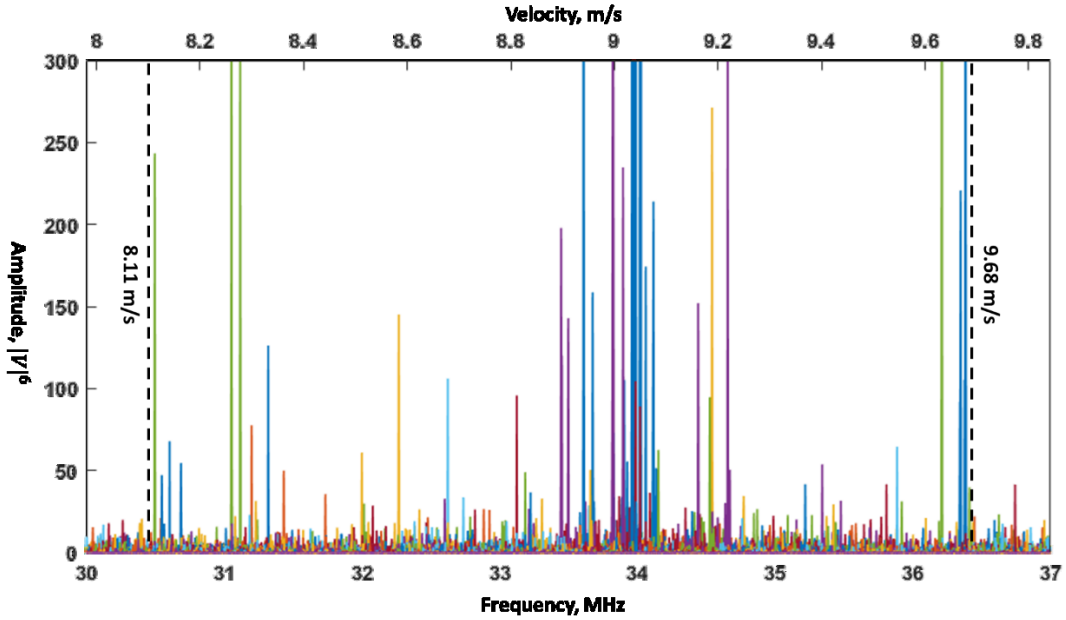

Figure 43. A zoomed in view of the low speed wind tunnel test section results.

The results of all wind tunnel tests performed with seeded flow are summarized below in Table 2, broken into low speed and high speed testing results. Each section displays the measured values made by the lidar system and the Pitot static tube with the percentage by which the lidar results varied from the Pitot static tube results. All but one test had lidar data varying from Pitot tube data by less than 1%, but all tests still matched the Pitot tube results to within its uncertainty. Table 2 shows that lidar testing inside the wind tunnel with tracer particles was successful.

Table 2. A summary of wind tunnel testing at all locations and speeds for seeded flow.

Low Speed

	A (m/s)	Pct. Diff.	B (m/s)	Pct. Diff.	C (m/s)	Pct. Diff.
Pitot Static Tube	7.5		8.3		8.9	
Lidar	7.51	0.1%	8.33	0.4%	8.98	0.9%

High Speed

	A (m/s)	Pct. Diff.	B (m/s)	Pct. Diff.	C (m/s)	Pct. Diff.
Pitot Static Tube	8		9		-	-
Lidar	8.09	1.1%	8.98	-0.2%	-	-

As hinted at with previous discussion, wind tunnel tests performed without tracer particles did not generate enough return signal to register any frequency peaks with a SNR greater than unity when performing the FFT. A representative plot of results without seeding the flow is shown in Figure 44. This plot shows results taken with the lidar system inside the test section at a low wind tunnel setting. Only 100 datasets were collected due to the lack of measurable results. In the frequency range of interest, no peaks in the FFT results had an amplitude greater than 100 or even seemed visible amongst the noise. Similar data was gathered when testing inside the inlet at low and high speeds.

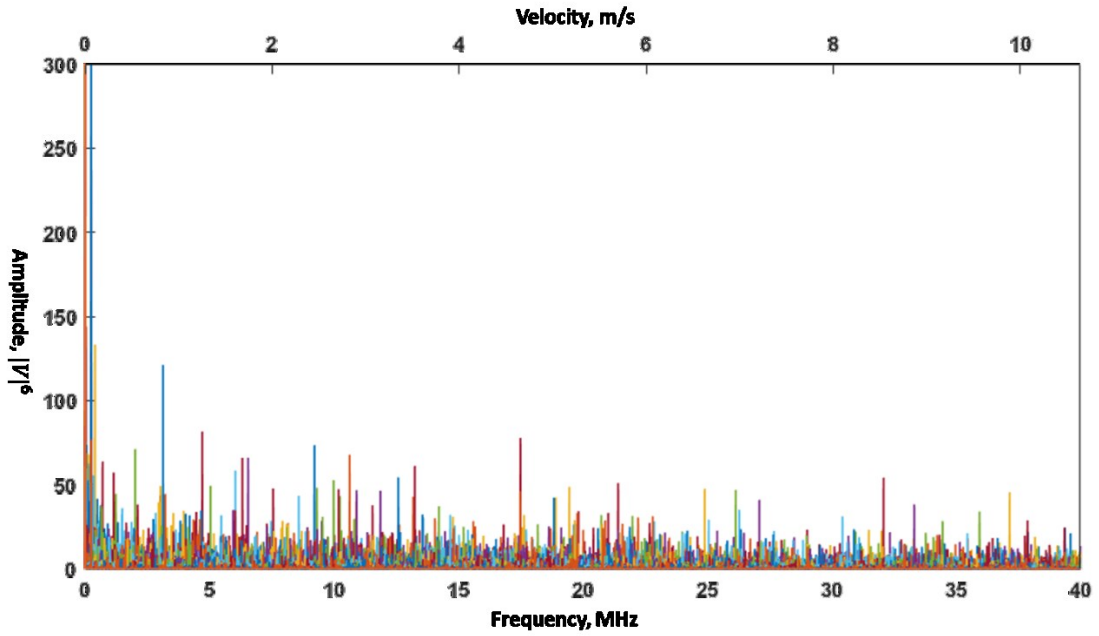

Figure 44. When the flow is not seeded, no velocity measurement can be made.

Several factors likely contributed to the overall reason why the photodetector could not measure the return signal without heavy seeding of the flow. First, several inefficiencies were not included in the original calculations. The laser power lost at each beamsplitter was ignored, and optical losses throughout the entire optical train due to reflections. Roughly 3.5% of light is reflected at each glass face for a 7% total loss due to each optical device. [68] Throughout the entire optical train, this equates to a total power loss of over 40%. This loss alone pushes the design point into the region requiring a Geiger mode photodetector for multiple speeds.

Two other inefficiencies in the system were discovered during the experimental setup process. The first of these which was already discussed, is the beam mixing efficiency. The return signal was not perfectly collimated when mixed with the LO at the secondary beamsplitter, so the two light sources did not focus to the same point after

passing through the final focusing lens in front of the APD. The high spatial frequency of interference fringes in Figure 30 is evidence of the low mixing efficiency. The number of fringes can be reduced by ensuring that the LO and signal are spatially matched. Finally, the two light sources focusing at different locations when travelling towards the APD caused a large amount of the return signal power to not hit the very small active area on the APD. Despite the return signal cross-sectional area shown in Figure 30 only being about 10% covered by the APD active area, an estimated 50% of the return signal reaching the photodetector is captured in the active area. This assumption is based on experience with seeing the output voltage of the APD when moving it horizontally and vertically across the return signal. Most of the return signal power is concentrated in the center of its cross-sectional area and can be captured by the APD.

In summary, the Doppler wind lidar system was able to successfully measure the Doppler shift (and therefore air velocity) caused by water vapor travelling through the inlet and test section of a small-scale wind tunnel. Measurements inside the wind tunnel matched well with Pitot static tube measurements. Tests performed with an ultrasonic transducer showed potential for the accuracy of the lidar system to be better than a Pitot tube and other velocimetry devices/methods. The current design was not sensitive enough to measure air speeds without the use of tracer particles, so a second iteration is necessary to improve the design.

CHAPTER VI

MODIFIED DESIGN OF COHERENT DOPPLER LIDAR

6.1 Lessons Inferred

Several valuable lessons were learned about the LIDAR setup and equipment that will be very helpful for future designers and experimentalists who might work on this research. The first lesson is that very precise spatial control of the optics is required to achieve proper alignment. Next, the optical system is very sensitive to vibrations and can be easily misaligned. If a commercial product is to be eventually made, the system must be more robust to the point that it can be easily moved around a wind tunnel without extensive realignment each time. Finally, a bistatic lidar system at these extremely short ranges becomes much more complicated since the collector lens and secondary beamsplitter must be well angled to collect and align the return signal with the LO.

6.2 Lidar Range Equation

These lessons learned and results of the experimentation were used to develop a second design iteration with an alternative methodology for estimating the lidar return power that is based on the lidar range equation. [58] The return power, *P,* of a lidar system is given by

$$P = K\ G\ \beta\ T \tag{20}$$

where K is the lidar system performance, G summarizes the range dependent geometry, β is the backscatter coefficient, and T is the transmission term. The lidar system performance is defined as

$$K = P_0 \left(\frac{c\tau}{2}\right) A\eta \tag{21}$$

The system performance relies on the output power P_0, the receiver area A, the time interval, (τ, pulse width for a pulsed laser and the detector integration time for a CW laser), and the system efficiency, η. The range dependent geometry is calculated as

$$G = \frac{O}{R^2} \tag{22}$$

where O is the receiver-field-of-view overlap function. The backscatter coefficient is

$$\beta = \sum\nolimits_j N_j \frac{d\sigma_{j,sca}}{d\Omega} \tag{23}$$

where N_j is the range dependent scattering particle concentration and $\frac{d\sigma_{j,sca}}{d\Omega}$ is the differential scattering cross section in the backward direction towards the receiver. Software called the Laser Environmental Effects Definition and Reference (LEEDR) was developed by the Air Force Institute of Technology (AFIT) Center for Directed Energy for atmospheric characterization. [69] The LEEDR software, run in Matlab, can estimate expected air properties including the backscatter coefficient. Finally, the transmission coefficient is given by

$$T = \exp\left[-2\int_0^R \alpha(r)dr\right] \tag{24}$$

where the extinction coefficient, α depends upon the laser wavelength and changes with measurement range, R.

To simplify this equation, several assumptions are made. First, when measuring at a range of only 1.5 meters, T is assumed to be unity. Next, O is also considered unity because the laser beam is completely imaged onto the detector. The lidar range equation then simplifies into

$$P = P_0 \frac{c\tau}{2} A\eta \frac{1}{R^2} \beta \tag{25}$$

Note that the return power is most sensitive to the measurement range. This is also true for the previous return power calculation method used.

The alternative return power estimation method is first applied to the current lidar design. The system efficiency includes a 10% loss at each of the two 90:10 beamsplitters, a 60% optical efficiency due to losses of light travelling through the optics (based on an estimated 7% loss caused by each optic [7]), and only 30% of the return light being incident on the photodiode active area caused by imperfect focusing of the return light (due to aberrations and misalignment, an estimation based on work discussed in Section 4.1). The inefficiencies discussed here total to a system efficiency of 14.6%. The magnitude of this efficiency is similar to other coherent lidar designs. [56] The current photodetector has a bandwidth of 400 MHz, so the measurement time interval is the inverse of this, $2.5\ x\ 10^{-9}\ sec$. The collector lens is 150 mm in diameter, and the laser in question is a 0.2 Watt CW laser operating at 532 nm. Based on use of the LEEDR software, the total backscatter coefficient at short range at the selected wavelength of 532 nm is estimated to be $2.4\ x\ 10^{-6}\ sr^{-1}$ (aerosol backscatter of $7.7\ x\ 10^{-7}\ sr^{-1}$ and a molecular backscatter of $1.6\ x\ 10^{-6}\ sr^{-1}$). This is based on the assumptions of a $70°F$ room temperature, 98.3 kPa pressure, relative humidity of 50%, and a typical indoor particle density of 5,600 cm^{-3}.

Using the simplified lidar range equation, this setup has an estimated return power of $2.06\ x\ 10^{-10}$ Watts. The APD has an integrated noise of $6\ x\ 10^{-9}$ Watts which gives a power ratio (between the return power and noise power) of only 0.034. [60] To get the power ratio to unity, a 5.9 Watt laser is required unless other components of the system are

modified. The return power estimated here is lower than the initial return power estimation by a factor of 313.

When adding water vapor to the air, there was cloud backscatter added to the aerosol and molecular backscatter which caused the total return power to be higher. Using the LEEDR software with fog conditions, the cloud backscatter coefficient is $7.4063\ x\ 10^{-4}\ sr^{-1}$ which causes the total backscatter coefficient to increase by a factor of over 300. The return power collected by the APD becomes $6.39\ x\ 10^{-8}$ Watts for a 0.2 Watt laser, which is a power ratio of 10.6. This signal is strong enough to be measured when performing an FFT of the acquired data.

6.3 New Lidar Design

Using these alternative equations, a new lidar system for wind tunnel measurements was designed. A schematic of the new monostatic design, reflective of other fiber optic designs, is shown in Figure 45. [70] [71] [72] Schematics of these similar designs are in Figure 46. These designs provided much of the inspiration for the second design iteration. The first major change to this design is the insertion of single mode fiber optics for better control of the light beams. Additionally, it is hypothesized that the mixing efficiency of the LO and return signal beams will improve when using fiber optics. The use of fiber to directly connect many components of the wind lidar system is expected to help make it more resistant to vibrations that can otherwise cause the optics to become misaligned. Testing performed with the current design was extremely inconsistent due to the ever changing alignment day to day. The use of fiber optics (which have a large power loss when coupling light into the fiber) is predicted to greatly reduce this problem. The two

beamsplitters for splitting and merging the beam were replaced by 99:1, 1:2 fiber optic couplers. Using a 99:1 ratio instead of 90:10 increases the return power by 17% alone. The laser, when upgraded to have 2 Watts of output power, increases the return power by one order of magnitude. Additionally, a circulator allows the system to be monostatic if the circulator can handle the laser power.

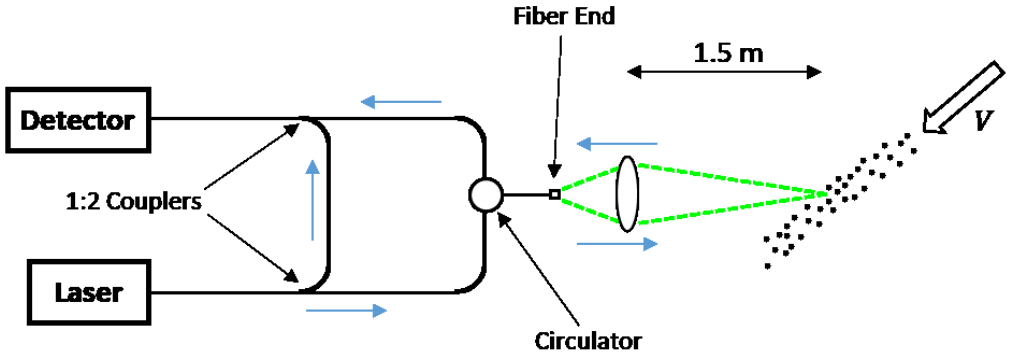

Figure 45. An alternative lidar velocimetry setup that relies on the use of fiber optics.

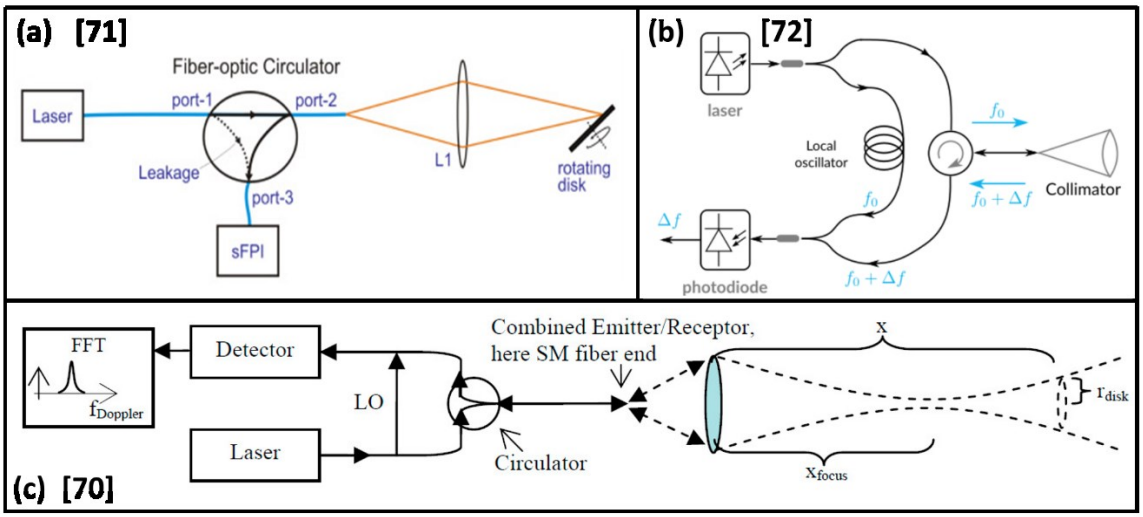

Figure 46. Multiple other wind lidar systems are bistatic and use fiber optics.

Another change in the design that significantly increases the return power is using a lower bandwidth photodetector. Reducing the bandwidth from 400 MHz to 100 MHz reduces the maximum measurable speed from 53.2 m/s to 13.3 m/s, but this should be enough for preliminary research. When working with a lower bandwidth, photodetectors typically have lower noise levels. Bandwidth of the previous testing was limited by the 100 MHz oscilloscope, so reducing the photodetector bandwidth to match the oscilloscope only helps the setup. An increase in the laser wavelength reduces the required photodetector bandwidth (via a reduction in the Doppler shift) per equation 9 to allow higher speed measurements, but molecular backscatter reduces with increasing wavelength to the fourth power per equation 15. For example, changing from a 532 nm laser to a 1550 nm laser would decrease the required detector bandwidth by a factor of about 2.9 but also reduce the return power by a factor of about 72. To measure higher velocities, a higher power laser is required. When these changes are made to the design (assuming a 60% fiber optic coupling efficiency and 80% system efficiency), the return power increases by a factor of 129 for a power ratio of 4.4.

Finally, a future iteration of the design presented here is to make it capable of measuring air speeds at multiple ranges. One way to do this is by switching from CW laser to a pulsed laser for range gating. Since the speed of light is known, the time required for an outgoing pulse to reflect off air molecules and return can be accurately calculated. The detector can be gated to collect light when the light from a specific measurement range is expected to arrive. One complication of using a pulsed laser is that the coiled fiber in the LO must be a variable length to ensure that the mixing light from the LO and the return signal are from the same laser pulse. They must travel the same distance, and this will vary

when measuring at different ranges. Additionally, the collector lens will not focus light properly to a point for passing back into the fiber optics. A device that can change focal length like a camera lens is required.

CHAPTER VII

CONCLUSIONS

The work presented in this thesis focused on the design and development of Doppler wind lidar for use as an alternative method for measuring air speeds in wind tunnels. Wind lidars are currently in use for many applications, but few investigations have been performed to study the use of these devices inside wind tunnels. No commercially available products currently exist as a wind lidar system specifically designed for wind tunnels. Current techniques for measuring velocities inside wind tunnels can be intrusive, require tracer particles, be complicated to perform properly, or not provide high accuracy measurements that are sometimes required. Doppler wind lidar has the capability to overcome all these problems and be a superior velocimetry technique.

After evaluating multiple design options, a coherent lidar system was constructed that utilized a 200 mW, CW laser with a 532 nm wavelength. Working in unison with a 400 MHz APD, the system could theoretically measure air speeds up to 53 m/s. Preliminary testing with an ultrasonic piezoelectric transducer proved that the system was capable of measuring a Doppler shift by generating a beat frequency between the LO and return signal. This test also showed that Doppler wind lidar has potential velocity measurement accuracy better than Pitot static tubes, hot wire anemometers, PIV, and LDV.

Initial testing of the lidar system proved that a simplified design can be used for velocity measurements of seeded flow inside a wind tunnel. These velocity measurements matched well with Pitot static tube data and showed potential for improving the accuracy of one-dimensional velocity measurements compared to Pitot static tubes and hot wire

anemometer. Unfortunately, only a small percentage of the captured dataset for a given test setup had a high enough SNR to measure a velocity. When the flow did not contain heavy seeding evenly spread throughout the entire 10 cm measurement region, the return signal was not strong enough to be measured by the photodetector.

A second iteration of the Doppler wind lidar system was designed for future use. The lidar range equation used in this design with updated information provided by AFIT appeared to provide a more accurate estimation of the power returning to the photodetector. This new design relies on fiber optics to minimize losses and create a more robust setup. Use of fiber optics with a more appropriate photodetector bandwidth and higher laser power is expected to create a large enough SNR for successful measurements of air speeds without relying on reflections from tracer particles.

Once the Doppler wind lidar design is properly modified to measure air speeds based solely on Rayleigh scattering, the system can be made more complex. The general theory has already been developed for velocity measurements with wind lidar systems through their use in studying flow at longer ranges. Some of these potential capabilities include measuring air speeds at multiple ranges inside a wind tunnel, scanning, and multiple systems working in unison to make three-dimensional velocity measurements. A compact Doppler lidar system that can make all of these measurements inside a wind tunnel cannot be matched by other velocimetry techniques.

REFERENCES

[1] J. D. Anderson, Jr., Introduction to Flight, Third ed., New York, NY: McGraw-Hill Book Company, 1989.

[2] P. M. Sholtis, "Characterization of Upstream Effects Due to High Blockage in the AFRL Vertical Wind Tunnel," University of Dayton, Dayton, Ohio, 2019.

[3] J. B. Barlow, W. H. Rae, Jr. and A. Pope, Low-Speed Wind Tunnel Testing, Third ed., New York, NY: John Wiley & Sons, 1999.

[4] Grainger Inc., "Data Logging Anemometer, 0 to 9999 fpm," Grainger Inc., [Online]. Available: https://www.grainger.com/product/TSI-ALNOR-Data-Logging-Anemometer-12A182?.

[5] Dantec Dynamics, "Measurement Principles of PIV," [Online]. Available: https://www.dantecdynamics.com/solutions-applications/solutions/fluid-mechanics/particle-image-velocimetry-piv/measurement-principles-of-piv/.

[6] Japan Aerospace Exploration Agency, "Optical Measurement Technologies," [Online]. Available: http://www.aero.jaxa.jp/eng/research/basic/aerodynamic/measurement/.

[7] M. Raffel, C. E. Willert, F. Scarano, C. J. Kahler, S. T. Wereley and J. Kompenhans, Particle Image Velocimetry: A Practical Guide, Springer, 2018.

[8] Dantec Dynamics, "Measurement Principles of LDA," [Online]. Available: https://www.dantecdynamics.com/solutions-applications/solutions/fluid-mechanics/laser-doppler-anemometry-lda/measurement-principles-of-lda/.

[9] A. Iannetti, R. Tacina, S. M. Jeng and J. Cai, "Towards Accurate Prediction of Turbulent, Three-Dimensional, Recirculating Flows With the NCC," American Institute of Aeronautics and Astronautics, Reno, Nevada, 2001.

[10] C. N. Raffoul, "A Three Component Laser Velocimetry Investigation of the Flowfield Downstream of a Bluff Body," University of Dayton, Dayton, OH, May, 1995.

[11] P. McManamon, LiDAR Technologies and Systems, Bellingham, Washington: Society of Photo-Optical Instrumentation Engineers, 2019.

[12] E. H. Synge, "A Method of Investigating the Higher Atmosphere," The London, Edinburgh, and Dublin philosophical Magazine and Journal of Science, 1930.

[13] E. A. Johnson, R. C. Meyer, R. E. Hopkins and W. H. Mock, "The Measurement of Light Scattered by the Upper Atmosphere from a Search Light Beam," Optical Society of America, 1939.

[14] M. A. Tuve, E. A. Johnson and O. R. Wulf, "Terr. Mag. 40, 452," 1935.

[15] E. O. Hulbert, "Observations of a Searchlight Beam to an Altitude of 28 Kilometers," Optical Society of America, 1937.

[16] W. E. K. Middleton and A. F. Spilhaus, "Meteorological Instruments," Toronto Press, Toronto, 1953.

[17] C. Weitkamp, "Lidar: Introduction," in *Laser Remote Sensing*, T. Fujii and T. Fukuchi, Eds., Boca Raton, FL: CRC Press, 2005, pp. 1-36.

[18] E. D. Hinkley, Laser Monitoring of the Atmosphere, Berlin, Germany: Springer, 1976.

[19] V. V. Gnidenko and V. O. Yatsenko, "LIDAR Hyperspectral System for Detecting Chemical and Biological Agents," in *Conference on Advanced Optoelectronics and Lasers*, Sudak, Ukraine, 2013.

[20] M. Luccio, "Lidar Innovations," Pale Blue Dot, LLC, Portland, Oregon, 2014.

[21] O. Cameron, "An Introduction to LIDAR: The Key Self-Driving Car Sensor," Voyage, 2017.

[22] M. P. Christiansen, M. S. Laursen, R. N. Jorgensen, S. Skovsen and R. Gislum, "Ground Vehicle Mapping of Fields Using LiDAR to Enable Prediction of Crop Biomass," in *14th International Conference on Precision Agriculture*, Montreal, Quebec, 2018.

[23] A. L. Thompson, K. R. Thorp, M. M. Conley, D. M. Elshikha, A. N. French, P. Andrade-Sanchez and D. Pauli, "Comparing Nadir and Multi-Angle View Sensor Technologies for Measuring in-Field Plant Height of Upland Cotton," *Remote Sensing,* vol. 11, no. 6, p. 700, 2019.

[24] G. W. Kamerman and D. V. Willetts, Military Remote Sensing, Bellingham, Washington: SPIE, 2004.

[25] G. D. Tzeremes, D. Jones, M. Hernandez, T. Sousa, A. Pollini, C. Pachel, J. Haesler and I. Carnelli, "Altimetry, Imaging and Landing Location Selection Lidars for ESA Space Applications," in *IEEE International Geoscience and Remote Sensing Symposium*, Yokohama, Japan, 2019.

[26] T. Z. Iverson, Signature Stability in Laser Doppler Vibrometry, Dayton, Ohio: University of Dayton, 2017.

[27] Hyperphysics, "Blue Sky," [Online]. Available: http://hyperphysics.phy-astr.gsu.edu/hbase/atmos/blusky.html.

[28] A. Melling, "Tracer Particles and Seeding for Particle Image Velocimetry," *Measurement Science and Technology,* vol. 8, no. 12, 1997.

[29] A. Cerny, P. Berger, M. Strizik, P. Engst and Z. Zelinger, "Differential Absorption Lidar (DIAL) Applied To The Mapping Of Horizontal Air Pollution Distribution: Examples From Measurement Campaigns In The Czech Republic," *Air Pollution,* vol. 66, p. 10, 20033.

[30] P. W. Chan, C. M. Shun and K. C. Wu, "Operation LIDAR-Based System for Automatic Windshear Alerting at the Hong Kong International Airport," in *12th Conference on Aviation, Range, & Aerospace Meteorology*, Atlanta, Georgia, 2006.

[31] A. Dolfi-Bouteyre, G. Canat and et al, "Pulsed 1.5-um LIDAR for Axial Aircraft Wake Vortex Detection Based on High-Brightness Large-Core Fiber Amplifier," *Journal of Selected Topics in Quantum Electronics,* vol. 15, no. 2, pp. 441-450, 2009.

[32] E. Cheynet, J. B. Jakobsen, J. Snaebjornsson, T. Mikkelsen, M. Sjoholm, J. Mann, P. Hansen, N. Angelou and B. Syardal, "Application of Short-Range Dual-Doppler Lidars to Evaluate the Coherence of Turbulence," *Experiments in Fluids,* vol. 57, no. 12, p. 184, 2016.

[33] S. Rahm, I. Smalikho and F. Kopp, "Characterization of Aircraft Wake Vortices by Airborne Coherent Doppler Lidar," *Journal of Aircraft,* vol. 44, no. 3, pp. 799-805, 2007.

[34] DTU Wind Energy, "WindScanner," [Online]. Available: http://www.windscanner.dk/specifications.

[35] Leosphere, "Windcube," Vaisala, [Online]. Available: https://www.leosphere.com/products/windcube/.

[36] S. Lugan and B. Michel, "The Green-Wake Project Targets both Air Traffic Security and Airport Throughput," 2013.

[37] N. Wildmann, S. Kigle and T. Gerz, "Coplanar Lidar Measurement of a Single Wind Energy Converter Wake in Distinct Atmospheric Stability Regimes at the Perdigao 2017 Experiment," *Journal of Physics Conference Series,* vol. 1037, no. 5, p. 052, 2018.

[38] N. Vasiljevic, G. Lea and et al, "Long-Range WindScanner System," *Remote Sensing of Wind Energy,* vol. 8, no. 11, p. 896, 2016.

[39] P. Fleming and et al, "Field Test of Wake Steering at an Offshore Wind Farm," *Wind Energy Science,* no. 1, pp. 229-239, 2017.

[40] ZX Lidars, "ZX TM - Turbine Mounted Wind Lidar," [Online]. Available: https://www.zxlidars.com/wind-lidars/zx-tm/.

[41] IRP Wind, "IRP Wind ScanFlow," [Online]. Available: https://www.irpwind-scanflow.eu/about/index.html.

[42] T. Mikkelsen, J. Mann, M. Courtney and M. Sjoholm, "Windscanner: 3-D Wind and Turbulence Measurements from Three Steerable Doppler Lidars," in *IOP*, 2008.

[43] Japan Transport Safety Board, "Aircraft Accident Information Database," Ministry of Land, Infrastructure, Transport and Tourism, 9 February 2010. [Online].

[44] N. P. Schmitt, W. Rehm, T. Pistner, H. Diehl, P. Nave and G. J. Rabadan, "A340 Flight Test Results of a Direct Detection Onboard UV Lidar in Forward-Looking Turbulence Measurement Configuration," in *15th Coherent Laser Radar Conference*, 2009.

[45] V. P. and et al, "Clear Air Turbulence Detection and Characterization in the DELICAT Airborne LIDAR Project," in *25th International Laser Radar Conference*, St. Petersburg, 2010.

[46] M. Garnet and A. Altman, "Identification of Any Aircraft by Its Unique Turbulent Wake Signature," *Journal of Aircraft,* vol. 46, no. 1, pp. 263-268, 2009.

[47] G. Ganci, A. Altman and J. Rodewald, "Identification of Aircraft by their Unique Turbulent Wake Signature: Experimental Validation," in *AIAA Aerospace Sciences Meeting and Exhibit*, Nashville, Tennessee, 2012.

[48] S. Gunasekaran and A. Altman, "Identification of Aircraft by their Unique Turbulent Wake Signature: Progress with Experimental Validation," in *AIAA Aerospace Sciences Meeting and Exhibit*, Grapevine, Texas, 2013.

[49] A. T. Pedersen and et al, "Demonstration of Short-Range Wind Lidar in a High-Performance Wind Tunnel," no. 3, pp. 1397-1402, 2012.

[50] M. F. Van Dooren and et al, "Demostration of Synchronised Scanning Lidar Measurements of 2D Velocity Fields in a Boundary-Layer Wind Tunnel," *IOP Journal of Physics: Conference Series,* vol. 753, no. 7, p. 72, 2016.

[51] J. D. Van de Hey, "Design, Implementation, and Characterisation of a Novel Lidar Ceilometer," Loughborough University, 2013.

[52] Y. Wang and et al, "Regularizing Method for the Determination of the Backscatter Cross Section in Lidar Data," *Optical Society of America,* vol. 26, no. 5, pp. 1071-1079, 2009.

[53] Circuit Globe, "Photodiode," [Online]. Available: https://circuitglobe.com/photodiode.html.

[54] Physics and Radio-Electronics, "Reverse Biased p-n Junction Diode," [Online]. Available: https://www.physics-and-radio-electronics.com/electronic-devices-and-circuits/semiconductor-diodes/reversebiaseddiode.html.

[55] K. Raghunath and et al, "Indo-Japanese Lidar Observations of Aerosols Over a Tropical Latitude," *Indian Journal of Radio & Space Physics,* vol. 29, pp. 239-244, 2000.

[56] T. Fujii and T. Fukuchi, Laser Remote Sensing, Boca Raton, FL: CRC Press, 2005.

[57] Malickova, Iveta and et al, "Laser Effect in the Optical Luminescence of Oxide Containing Cr," *ACTA Geologica Slovaca,* vol. 10, no. 1, pp. 27-34, 2018.

[58] C. Weitkamp, Lidar: Range-Resolved Optical Remote Sensing of the Atmosphere, Geesthacht, Germany: Springer, 2005.

[59] Cobolt Lasers, "DPSS Lasers - SLM Laser," [Online]. Available: https://www.coboltlasers.com/lasers/dpss-lasers-single-frequency-cw-diode-pumped-lasers/.

[60] Thorlabs, "Si Avalanche Photodetectors," [Online]. Available: https://www.thorlabs.com/thorproduct.cfm?partnumber=APD430A2.

[61] FLIR Systems, Inc., "Grasshopper3 USB3," [Online]. Available: https://www.flir.com/products/grasshopper3-usb3/?model=GS3-U3-23S6M-C.

[62] STEMiNC, "Ultrasonic Transducer for Massage 5 MHz," [Online]. Available: https://www.steminc.com/PZT/en/ultrasonic-piezo-transducer-for-massage-5mhz?gclid=EAIaIQobChMI3Yzgn4i65AIVyJyzCh2J4QAFEAkYAiABEgIwPvD_BwE.

[63] A. A. Fedorets and et al, "Self-Assembled Levitating Clusters of Water Droplets: Pattern-Formation and Stability," *Scientific Reports, a Nature Search Journal,* vol. 7, no. 1888, 2017.

[64] C. Tropea, A. Yarin and J. F. Foss, Handbook of Experimental Fluid Mechanics, Springer, 2007.

[65] J. W. Woodman, Introduction to Fourier Optics: Third Edition, Englewood, Colorado: Roberts & Company, 2005.

[66] D. E. Newland, An Introduction to Random Vibrations and Spectral Analysis: Second Edition, New York, New York: Longman Scientific & Technical, 1984.

[67] MathWorks, "fft," [Online]. Available: https://www.mathworks.com/help/matlab/ref/fft.html.

[68] M. Raffel and et al, Particle Image Velocimetry: A Practical Guide, Springer, 2018.

[69] J. Schmidt, "LEEDR User Guide Version 4.00.029," Air Force Institute of Technology, Center for Directed Energy, Dayton, Ohio, 2019.

[70] C. Hill, "Coherent Focused Lidars for Doppler Sensing of Aerosols and Wind," Multidisciplinary Digital Publishing Institute, Worcestershire, United Kingdom, 2018.

[71] P. J. Rodrigo and C. Pederson, "Monostatic Coaxial 1.5 um Laser Doppler Velocimeter Using a Scanning Fabry-Perot Interferometer," Optics Express, Roskilde, Denmark, 2013.

[72] Koheron, "Build a Doppler Lidar Velocimeter," 2015. [Online]. Available: https://www.koheron.com/blog/2015/11/15/doppler-lidar-velocimeter.